END
DATE
FILMED
9 85

UNLIMITED

ROYAL AIRCRAFT ESTABLISHMENT

STUDIES OF THE FLOW FIELD NEAR A NACA 4412 AEROFOIL
AT NEARLY MAXIMUM LIFT

by

R. C. Hastings

B. R. Williams

December 1984

DTIC

R O Y A L   A I R C R A F T   E S T A B L I S H M E N T

STUDIES OF THE FLOW FIELD NEAR A NACA 4412 AEROFOIL
AT NEARLY MAXIMUM LIFT

by

R. C. Hastings

B. R. Williams

SUMMARY

Measurements made at a Mach number of 0.18 and a chord-based Reynolds number of 4.2×10^6 on a constant-chord model having a NACA 4412 aerofoil section are described and compared with the results of flow field calculations.

Both the experimental arrangement and the difficulties initially experienced in achieving an adequate approximation to two-dimensional flow above the wing are briefly outlined.

The measurements include static pressure distributions on the wing surface and on the wind tunnel walls above and below the mid-span section of the wing. The main emphasis in the experiment was, however, on defining the development of the upper surface boundary layer through separation (at about 20% chord ahead of the trailing-edge) and on into the wake, making extensive use of laser anemometry.

The flow field calculations are of the semi-inverse kind in which an inverse momentum-integral treatment of the shear flow, used to avoid difficulties at separation, is coupled to a direct solution of the inviscid flow problem. The main features of the method are outlined.

LIST OF CONTENTS

1 Introduction

It is now well established that flows past many types of bodies on which there are attached boundary layers can be computed in a variety of ways[1] and intensive efforts are now being made to extend computational capability to cover flows containing regions of flow separation. Such extensions will clearly have considerable practical impact on aerodynamic design. One example, with which the present work is concerned, occurs in aerofoil profile development where the ability to predict the stalling behaviour of given aerofoils will be most valuable.

A technique which has proved successful in the estimation of the effects of viscosity in the attached flow around aerofoils is to match a calculation of the outer inviscid flow with a calculation of the boundary layer development on the surface of the aerofoil. In a recent paper Williams[2] has drawn attention to certain obstacles to the extension of this technique to separated flows and illustrated ways in which they may be overcome in calculations for incompressible inviscid outer flow. Although most of the impediments are related to the nature of the calculation procedure and have to be tackled by adopting suitable strategies in formulating computational methods, the adequate modelling of both the separated parts of boundary layers on aerofoils and of their wakes also presents difficulties.

Information obtained from experiment is a prerequisite to the solution of these viscous flow problems. The first four of the following Sections are devoted to an experiment designed to provide such information for the particular case of an NACA 4412 aerofoil tested at an incidence close to that for maximum lift. This provides an example of the type of stall which develops with increasing incidence by the progressive enlargement of a region of separated flow on the rear part of the upper surface of the aerofoil. An additional reason for choosing the NACA 4412 section for the experiment was to create an opportunity for comparing results with other work such as that of Wadcock[3]. Some comparisons, not repeated here, with Wadcock's work for both theory and experiment are included in Refs 2 and 4. Ref 4 also gives additional details of the RAE experiment.

In the second part of the paper a theoretical method for computing flows containing regions of separation is described and its predictions are compared with the experimental results.

2 Experimental Details

The experiment was performed in the 13ft × 9ft (4 m × 2.74 m) Low Speed Wind Tunnel of the Royal Aircraft Establishment at Bedford. This facility is a conventional, closed-circuit, wind tunnel with excellent flow quality, operating at atmospheric pressure. The tunnel is large enough to accommodate models of sufficient size to permit detailed study of their flow fields.

In this case the model has a constant chord of 1 m, a NACA 4412 aerofoil section and spans the full width (4 m) of the tunnel. It is mounted with its quarter-chord point, about which it pivots in the pitch plane, on the tunnel centre line. It is extensively instrumented with static pressure orifices. Boundary layer and wake measurements were made at mid-span where the main chordwise set of 88 pressure orifices is located.

When first tested at an incidence of approximately 14°, the model was found to have strongly three-dimensional flow over the rear part of its upper surface; elsewhere the flow was very well-behaved. Surface oil-flow studies revealed that the three-dimensional flow near the surface of the wing was composed of the kind of cellular entities which are now recognised to be fairly common[5] in separated flows. A short leading-edge separation bubble was also detected, separation and reattachment being roughly at 1% and 1.7% chord respectively. As the overriding consideration in this experiment was to obtain laser anemometer measurements in two-dimensional, separated, mean flow it was imperative to take measures to control the flow without impeding optical access to the mid-span part of the model.

Further oil-flow studies indicated that the natural flow on the model was very close to being two-dimensional up to an incidence of 11° where

separation was at about 90% chord. It was found that the region of acceptable flow quality could be extended to 13° by adding judiciously-placed, streamwise fences running around the leading edge of the wing and continuing along the front half of its upper surface. The most important fences were a pair symmetrically placed on either side of mid-span and 1.7 chords apart. Because cellular stall patterns appeared in the spaces between these fences and the sides of the tunnel, an additional fence was placed in each of these spaces to split and weaken these outboard cells. The additional fences were 1.5 chords from mid-span.

It was also considered possible that there might be irregularities in the leading-edge bubble separation and reattachment process that could be partly responsible for the development of three-dimensionality in the flow further downstream. To counter this possibility an unusually wide, boundary layer tripping band was fitted to the upper surface. This consisted of densely packed, 0.28 mm diameter (0.011 in) ballotini attached by a thin layer of adhesive. The band extended 30 mm along the aerofoil contour from the leading-edge; ie to 1.4% chord along the chord line. Transition was fixed on the lower surface by a similar, but much narrower, band extending from 10% to 11% of the chord.

A geometric incidence of 12.15° was finally selected for the main series of tests so that the flow would be steadier than at 13°, where continuous visual observation of developing oil-flow patterns had indicated that the flow over the rear part of the wing contained complicated transient phenomena. The undisturbed free stream speed for the tests was 61 m/s, stream temperatures (which are not controllable) were 22 ±10° C, while the Mach and Reynolds numbers were 0.18 and 4.2 × 10^6 respectively. Apart from the main tests, there were subsidiary tests at lower incidences to define the aerofoil's lift curve.

The main instrument used for studying the boundary layers and wakes was a two-component, photon-correlation, laser Doppler anemometer (LDA). This was operated in back-scatter and was mounted on a traverse mechanism situated just outside the tunnel and to starboard of the model. Frequency-shifting by Bragg cells was incorporated to resolve directional ambiguities in measured velocities. The two output signals for each measurement were fed first to separate autocorrelators and thence to a digital computer for storage and processing. The end-products were probability distributions for the magnitudes of the two, always orthogonal, velocity components that were being measured.

The anemometer is designed so that the orientation of the pairs of velocity components can be varied. Components inclined both at 0°, 90° and ±45° to the line of traverse were always measured. In principle this should enable the shear and normal components of Reynolds stress in the plane of the mean, two-dimensional flow to be evaluated; in practice difficulties were encountered which are attributable ultimately to the remoteness of the anemometer from the measuring plane coupled with various practical constraints on the geometry of the optical system[4]. Consequently only mean velocity data from the LDA are presented here. The

measuring region yielding each data point has an effective diameter of 2 mm (less than 1/30 of the thickness of the separated boundary layer) in the plane of the mean flow and extends about 20 mm spanwise. Here again the size of the measuring region is related to its distance from the anemometer.

The boundary layer and wake were always traversed along lines normal to the wing surface and to the (extended) wing chord line, respectively. The air stream was seeded with atomised oil droplets introduced at the downstream end of the working section of the tunnel.

To compensate as far as possible for the lack of Reynolds stress data from the laser anemometer, some additional traverses with hot-wire probes were made. These probes were mounted or a long arm projecting forward from a precision traverse gear[6] originally built some years earlier for other work on wakes. The same equipment was used to obtain velocity profiles from pitot tube surveys at 20% and 40% chord on the upper surface and at 99.7% chord on the lower surface.

3 Wind Tunnel Boundary Conditions and Interference

Table 1 lists static pressures measured on the longitudinal centre-lines of the roof and floor of the working section. These pressures have been used in conjunction with the method of Ashill and Weeks[7] to find the tunnel-wall-induced velocity perturbations midway between the tunnel roof and floor for plane flow. As well as an average blockage-induced, velocity increment of $0.0073U_\infty$ (for an undisturbed flow speed of U_∞) there exist both a mean induced inclination of the stream of about 0.34° and a curvature equivalent to a camber of -0.28%. Fig 1 shows the induced upwash (w_i/U_∞) and streamline ordinates (z_i/c).

The boundary layers on the roof and floor of the empty working section 3.29 m ahead of the position of the model's leading edge have the following characteristics: displacement thickness (δ^*) = 7.6 mm, Reynolds number for momentum thickness $\theta = 24400$, shape parameter H (H = δ^*/θ) = 1.30.

4 Measured Wing Static Pressure Distribution

The pressure distribution around the aerofoil profile at mid-span is shown in Fig 18 where it is compared with the results of calculations to be described in Sections 6 and 7. The measurements do not define the pressure distribution just behind the leading edge well enough to yield extremely accurate force coefficients at high incidences. It is believed that the lift coefficient is $C_L = 1.46 \pm 0.01$ at the incidence of 12.15° for the main series of tests.

At this incidence, pressures were very accurately repeatable over the whole of the lower surface of the wing, where the pressure gradients were all favourable, and also if x/c was less than 0.45 on the upper surface (x being measured along the chord line of length c). Further downstream on the upper surface differences between repeated measurements began to appear. These differences may be attributed to some unsteadiness in the

flow, for which there was visual evidence as noted in Section 2. Just ahead of separation the scatter indicated by four repeated measurements is 0.025 in C_p. At the same station, x/c = 0.75, the static pressure data from a spanwise row of measuring orifices fell within a band whose width is 0.06 in C_p for stations within ±0.6 c of mid-span. This figure includes both scatter and small systematic spanwise variations. Although the chordwise pressure distribution is not tabulated in detail, values of C_p at boundary layer traverse stations are included in Table 2.

5 Boundary Layer and Wake Measurements

Fig 2 gives a general impression of the scope of the boundary layer and wake velocity profile measurements. Leading characteristics of the profiles are listed in Tables 2 and 3 for the boundary layers and wake in turn. As may be seen from Fig 2, boundary layer separation was found to be at approximately x/c = 0.8 on the upper surface. Fig 3 shows four mean velocity profiles obtained by laser anemometry in the separated boundary layer on two different occasions and with two laser beam orientations. The later measurements are rather more consistent because the anemometer has been progressively improved during the course of the experiment. Normalised profiles for 0.66 < x/c < 0.997 are shown in Fig 4. The velocity component parallel to the wing surface (U) is given as a fraction of U_e its value at the edge of the boundary layer; distance (n) normal to the wing surface is given as a fraction of δ, its value when U = 0.995 U_e; in the interests of clarity smoothed profiles and not individual data points are shown. The shapes of the profiles change in an orderly way as separation is approached and passed. It is worth noting that there are measurable velocity gradients normal to the wing surface in the inviscid flow outside the boundary layer.

The presence of these velocity gradients is an indication that the boundary layers are too thick for classical first-order boundary layer theory to apply and highlights the importance of taking account of higher order effects in the calculations which are described in Sections 6 and 7. There is the further implication that generalised definitions of boundary layer displacement and momentum thicknesses should be used in the presentation of experimental data. It should be noted that this has not yet been done for the data of this experiment; ie the quantities ρ_i and U_i of the equivalent inviscid flow (EIF) of Sections 6.1 and 6.2 have been taken to be respectively a constant (for this low Mach number flow) and U_e in analysing the data.

It may be seen from Fig 3 that the mean velocity profiles are subject to some uncertainty, particularly near the wing surface; this affects the derived values included in the Tables. Momentum thickness is the quantity most seriously affected. Examination of the data suggests that δ, δ^*, θ and H are subject to the following maximum uncertainties: ±5%, ±3%, ±8% and ±8% respectively.

The mass flow shape parameter $[H_1 = (\delta-\delta^*)/\theta]$ can also be determined. Values of H_1 from this experiment are in satisfactory agreement with the curve of Fig 14 for attached flow; for separated

flow, however, smoothed values of H_1 appear to remain constant at H_1 = 4 when H exceeds 5. In order to reproduce the rising trend in Fig 14, values of δ that gradually exceeded the experimentally-derived ones would have to be chosen; for example the required increment would be 10% at H = 7.5. With regard to this observation, it is worth noting two points. Firstly the curve passes through H_1 = 4 at H = 4 which is consistent with a cosinusoidal wake-like profile if δ is defined to be where U = U_e. This version of δ exceeds δ for U = 0.995U_e by almost 5% for that profile. Secondly we have noticed a consistent tendency for U, if it is very close to U_e, to approach U_e rather more quickly when, as here, it is measured by a laser anemometer than when it is measured by an (intrusive) hot-wire probe and so the laser-derived boundary layer thicknesses may be slightly less than those that other instruments would yield.

Skin friction coefficients for the attached-flow boundary layers have been estimated by the Clauser chart method (for a Karman constant of 0.41 and an additive constant of 5.2 in the logarithmic part of the velocity profile), though only within rather broad limits for flows near separation where the logarithmic parts of the profiles are very small. If we denote the skin friction coefficient and the value predicted by the well-known Ludwieg and Tillmann formula by c_f and c_{fL} respectively, the results are well represented by the interpolation formula c_f = 0.985 c_{fL} − 3 × 10⁻⁵. This relationship is consistent with a value of 4 for H at separation in this experiment. The estimates of c_f are included in Table 2.

Reynolds stresses in the outer parts of the boundary layers were measured with a hot-wire anemometer. Comparison of mean velocity profiles obtained by the wire and laser anemometers showed that there were probe interference effects on the former and so the Reynolds stresses are presented in Figs 5 and 6 only for the parts of the boundary layers where the two types of anemometer yielded mean velocity profiles of very similar shapes.

The dimensionless normal stresses $\overline{u^2}/U_e^2$ and $\overline{w^2}/U_e^2$ progressively increase in importance from x/c = 0.59 to the trailing-edge of the wing. In contrast the peaks of the dimensionless shear stresses initially increase but soon reach a maximum, at which they remain from at least x/c = 0.66 to x/c = 0.85, before falling slightly near the trailing edge. Peak shear stress coefficients,

$$(c_\tau)_{max} = (-2\overline{uw}/U_e^2)max,$$ are included in Table 2.

Since the normal stresses are clearly of increasing importance to the overall momentum balance of the boundary layer near and beyond separation, an attempt, recorded in the final column of Table 2, has been made to estimate their contribution to the momentum integral equation. The estimate relies on the assumptions that the shapes of the distributions of $(\overline{u^2} - \overline{w^2})/U_e^2$ are mainly functions of $(H-H_o)/H$ and may be scaled by using the maximum values of $(\overline{u^2} - \overline{w^2})/U_e^2$. H_o is the value of H in a datum equilibrium flow with zero pressure gradient at the relevant local value of R_θ. The tabulated quantity I/θ is defined by

$$I/\theta = \frac{1}{\theta} \int_o^\delta \frac{\overline{u^2} - \overline{w^2}}{U_e^2} \, dn \ .$$

Its algebraic significance is that one may regard it as reducing θ to $\theta(1 - I/\theta)$ in the conventional momentum integral equation. This may be written[1], with normal stresses (but no other higher-order terms) included, as

$$\frac{d}{dx} \left[U_e^2(\theta - I) \right] + \delta^* \frac{d}{dx}(\tfrac{1}{2}U_e^2) = \tfrac{1}{2}c_f U_e^2 \ ;$$

here I is the normal stress integral defined above. Integrating from an initial station x_1 to x, and dividing by the value of $U_e^2 \theta$ at x_1, we obtain

$$\frac{U_e^2(\theta - I)}{(U_e^2 \theta)_1} - 1 = \frac{1}{2(U_e^2 \theta)_1} \int_{x_1}^x \left[c_f U_e^2 - \delta^* \frac{dU_e^2}{dx} \right] dx \ ;$$

if I is negligible at x_1.

A momentum balance for the upper surface boundary layer is given in Fig 7. A datum at $x/c = 0.2$ has been chosen. The positive contribution is $U_e^2 \theta / (U_e^2 \theta)_1 - 1$, shown by solid lines. The effect of modifying θ to take account of normal stresses as just previously outlined is indicated by broken lines. The balancing contributions (below the x/c axis) comprise

$$\frac{1}{2(U_e^2 \theta)_1} \int_{0.2c}^x \left[c_f U_e^2 - \delta^* \frac{d U_e^2}{dx} \right] dx.$$

The flow is seen to be nearly in balance in general and so should represent a good approximation to two-dimensional mean flow; however the scatter of the values of θ and δ^* makes it difficult to draw firm conclusions. Beyond separation ($x/c = 0.8$) the contribution of the estimated normal stresses is significant and it would clearly be worthwhile to incorporate estimates of other higher order effects.

The development of the upper surface boundary layer is illustrated in quantitative terms in Figs 16, 20 and 21. The displacement thickness grows steadily along the chord and does so particularly rapidly near and beyond separation (Fig 20). This leads to a rapid increase in H (Fig 21) over the rear part of the chord because θ (Fig 16) varies comparatively slowly aft of separation.

The wake has been divided into upper and lower parts by estimating the position of the mean streamline separating the flows that have passed above and below the wing. This was done by considering the mass flux into and within the lower and thinner part of the wake on the assumption that the mean flow was two-dimensional. Dimensionless velocity profiles for both parts of the wake, similar to those given in Fig 4 for the wing boundary layer, are shown in Figs 8 and 9. Dimensionless velocities at the edges of the wake and on its internal dividing streamline are given in Fig 10.

It can be seen from Fig 10 that there is some pressure recovery in the near wake, to slightly beyond the value in the undisturbed stream. The velocities on the dividing streamline at stations close to the wing are scattered and unreliable because the velocity gradients are very steep and so a very slight change in the position of the streamline has a disproportionately large effect on the estimated velocity. Further downstream the velocity on the dividing streamline increases as mixing begins to equalise the velocities within the wake.

Since the upper and lower parts of the wake are derived respectively from a very thick separated boundary layer and a very thin attached boundary layer they are initially very different and both change markedly just behind the wing. Reversed mean flow persists in the upper part of the wake until x/c reaches 1.09. As Fig 11 shows, the displacement thickness (δ_u^*) of the upper wake falls and that (δ_l^*) of the lower wake rises in this region. The corresponding momentum thicknesses θ_u and θ_l do not change as smoothly. The former has a maximum near $x/c = 1.2$. This is tentatively associated with the closure of the bubble of reverse flow. This interpretation is consistent with results obtained by Green[9] in an attempt to model a flow that is qualitatively similar in some respects - namely reattachment behind a rearward-facing step. He found that θ peaked in his calculations at a point of maximum static pressure just beyond reattachment. The peak found in this experiment is likewise beyond bubble closure and roughly where the near-wake pressure recovery ends (Figs 2 and 10).

The displacement surfaces above the rear part of the wing and in the wake are included in Fig 2. Despite the rapid variations in displacement thickness near the trailing edge, the upper displacement surface is smooth and only slightly curved. The net effect of the displacement surfaces on the outer inviscid flow is equivalent to a reduction in camber and in increase in thickness near the trailing edge. The wake is noticeably inclined to the wing chord line within the range of the measurements. Table 3 includes the estimated position of the dividing streamline in the wake.

6 General Description of the Prediction Method for Separated Flow

A viscous-inviscid interaction method is used. It differs from the type that is successful in treating attached flow, for which it has been shown[1] that the effects of viscosity can be estimated by coupling a solution of the outer inviscid flow with a direct solution for the boundary layers and wakes associated with an aerofoil. For a direct solution of the boundary layer, the pressure distribution is specified and the displacement thickness (among other quantities) is calculated. As the boundary layer approaches separation the equations describing it become stiff[10] in the sense that a small change in pressure distribution leads to a large change in displacement thickness. This stiffness leads to numerical problems in the integration of the equations, thus limiting the approach described in Ref 1 to attached flows. If the boundary-layer equations are solved in inverse form - ie the pressure distribution is calculated from, say, the displacement thickness, then close to separation the equations are no longer stiff and integration of the equations presents no numerical difficulties. An integral formulation of an inverse turbulent-boundary layer method is given by East

et al[11] and is derived from the direct lag-entrainment method given by Green et al[12]: an extension of this inverse method is used in the present calculation.

The inverse solution of the boundary layer equations is matched to a direct calculation of the inviscid flow by a semi-inverse scheme of the sort described by Carter[13] and Le Balleur[14]. A full description of the method is given in Refs 2 and 15, but an outline of the method is given in the following sections. First a description of the boundary conditions and the calculations for the outer inviscid flow is given. This is followed by a description of the boundary layer equations including some second order terms and the modifications needed for separated flow. Finally a description of the semi-inverse scheme and a relaxation formula derived from a stability analysis are presented.

6.1 Boundary Conditions for the Outer Inviscid Flow

Ref 1 describes the matching of flows including the effects of higher-order terms; these terms become more important in separating and separated flow. In the matched solution it is assumed that the flow field can be split into two regions; an inner region described by the Navier-Stokes equations (or some approximation of these equations) and an outer region described by the Euler equations, which for irrotational incompressible flow are approximated by Laplace's equation. If an integral formulation is used to describe the development of the boundary layer then it is most convenient to match the inner and outer solutions on the aerofoil surface and some convenient line in the wake: the definition of the inviscid flow is extended through the boundary layer and wake to this matching line. Following Lock and Firmin[1] the new inviscid flow is called the equivalent inviscid flow (EIF) whilst the name real viscous flow (RVF) is reserved for the physical flow. The boundary conditions for the EIF are obtained by differencing continuity and momentum equations for the EIF and RVF, (the 'deficit formulation') and are summarised in Fig 12. The transpiration velocity W_{iw} is given exactly by differencing the continuity equation for the RVF and EIF, then integrating the difference across the shear layer, to give

$$W_{iw} = \frac{1}{\rho_{iw}} \frac{d}{ds} \left(\rho_{iw} U_{iw} \delta^* \right) \qquad (1)$$

with[8] $\delta^* = \frac{1}{\rho_{iw} U_{iw}} \int_0^\infty (\rho_i U_i - \rho U) dn$ and s, n as

distance along and perpendicular to the surface, where suffices i and w indicate the equivalent inviscid flow and conditions at the surface of the aerofoil respectively. Other symbols take the usual meaning, U, W as velocity along s and n, ρ as density and δ^* as a displacement thickness.

By neglecting small terms in the integrated form of the difference of the normal momentum equation for the EIF and RVF, a simple numerical approximation for the difference in wall pressure between the EIF and RVF is derived as[8]:

$$\frac{P_{iw} - P_w}{\rho_{iw} U_{iw}^2} = K^*(\theta + \delta^*) \qquad (2)$$

where K^* is the curvature of the displacement surface and θ is the momentum thickness of the boundary layer. Thus the pressure calculated in the EIF has to be corrected before comparison with experimental values.

In the wake similar boundary conditions apply on a convenient line dividing the flows from the upper and lower surfaces of the aerofoil. It is helpful in some ways to regard this line as a vortex sheet in the EIF and refer to it as such. The displacement effect of the wake is given by a jump ΔW, in the component of velocity normal to the wake, which by analogy with equation (1) is given by

$$\Delta W_i = \frac{1}{\rho_{iw}} \frac{d}{ds} \left(\bar{\rho}_{iw} \bar{U}_{iw} \delta^*_t \right) \qquad (3)$$

where suffix t denotes the total for the wake and $^-$ denotes mean values.

The pressure variations across the wake in the RVF and EIF are different. The flows outside the wake are matched by placing a vortex sheet in the wake in the case of the EIF. By integrating the difference forms of the normal momentum equation for the EIF and RVF across the wake, the pressure difference across the vortex sheet is found to be:

$$\Delta p_i \equiv p_{iu} - p_{il}$$

$$= K_w \bar{\delta}_{iw} \bar{U}_{iw}^2 \left(\delta^*_t + \theta_t \right) \qquad (4)$$

where $^-$ denotes mean values and K_w is the curvature of the dividing streamline.

6.2 Outer Calculation: Equivalent Inviscid Flow

Although the matching scheme will allow solutions for compressible flow, for the present low-speed calculations about a NACA 4412 aerofoil the outer flow is assumed to be incompressible and irrotational and is given by a solution of Laplace's equation. The outer-flow problem is now linear and a solution of the EIF is obtained without iteration. Through Green's third identity the solution of Laplace's equation can be expressed as a combination of fundamental solutions distributed on the surface of the aerofoil. In two dimensions the fundamental solutions are taken as sources and vortices and are approximated by piecewise continuous functions defined on the N sides of a polygon inscribed in the aerofoil (see Fig 13). A numerically stable scheme, developed by Newling[16], has the source distribution as constant on each panel and the vorticity varying linearly. The particular mix of sources and vortices is chosen so that the singularity densities on opposite panels on the upper and lower surface are equal. The number of unknowns is N+1 of which N are determined by satisfying a Neumann boundary condition at the centre of each panel, that the normal velocity should be given by equation (1). The final unknown is the strength of the vorticity at the trailing edge and smooth flow at the trailing edge is obtained by setting the vorticity on the aerofoil at the trailing edge equal to the vorticity obtained by approaching the trailing edge from upstream through the wake: the value is obtained from equation (4).

The shape of the streamline in the EIF from the trailing edge is calculated by an interactive process. An initial guess at the shape of the

streamline is split into panels and, by sweeping down the wake, each panel is progressively aligned with the local flow direction. In the wake the boundary conditions for the EIF are represented by constant source panels along the dividing streamline for the displacement effect and linearly varying vorticity for the curvature effects. The strengths of the sources and vortices are derived from equations (3) and (4) respectively. In the present method it has not been possible to obtain converged solutions with a representation of the curvature effects in the wake, so all the calculations reported have the vorticity in the wake set to zero.

6.3 Inner Calculation: Shear Layer

A set of integral equations for calculating the development of a turbulent boundary layer is given by Lock[1]. These equations use a normalised transpiration velocity $S = 1/\rho_{1w}U_{1w}d/ds(\rho_{1w}U_{1w}\delta^*)$ as independent variable as opposed to the displacement thickness used by East et al[11]. Both integral formulations require a correlation between the shape factors

$$\bar{H} = \frac{1}{\theta}\int_0^\delta \frac{\rho}{\rho_{1w}}\left(1-\frac{U}{U_{1w}}\right)dn \text{ and } H_1 = \frac{1}{\theta}\int_0^\delta \frac{\rho U}{\rho_{1w}U_{1w}}dn .$$

In the integrals above, the upper limit δ is the true edge of the boundary layer, not where $U = 0.995U_e$ as in the presentation of the experimental results in earlier Sections.

The new set of equations based on S permits the use of a correlation which has a minimum close to separation and which consequently accords more closely with experimental measurements of separating flow. The new equations also include higher order terms as proposed by Weeks[17]. The four equations are given below.

Streamwise Momentum Integral Equation

$$\frac{d\theta}{ds} = \frac{c_f}{2} - (H+2-M^2)\frac{\theta}{U_{1w}}\frac{dU_{1w}}{ds} - \frac{1}{\rho_{1w}U_{1w}^2}\frac{d}{ds}(\rho_{1w}U_{1w}^2 f\theta)$$

where c_f is the skin-friction coefficient, M is the local Mach number; f embodies the second order terms as $f = K^*(\theta+\delta^*)/2\theta - (I/\theta)C_\tau/C_{\tau EQ}$ with I as the Reynolds normal stress integral $\int_0^\delta[(\overline{u^2}-\overline{w^2})/$ $U_{1w}^2]dn$, C_τ the shear stress coefficient and $C_{\tau EQ}$ its value in equilibrium conditions. The equation can be reduced to standard form by defining

$$\tfrac{1}{2}c_f^* = \tfrac{1}{2}c_f - \frac{1}{\rho_{1w}U_{1w}^2}\frac{d}{ds}(\rho_{1w}U_{1w}^2 f\theta) .$$

Entrainment Equation

$$D\theta\frac{d\bar{H}}{ds} = H_1 S - \frac{1}{5}M^2 H_1 c_f^* - C_E(\bar{H}-\tfrac{2}{3}M^2)$$

where C_E is the entrainment coefficient and $D = H_1 - H \, dH_1/d\bar{H} + (H_1+2dH_1/d\bar{H})M^2/5.$

Lag-entrainment Equation

$$\frac{\theta dC_E}{ds} = F(C_E,c_{fo})\frac{2.8}{H+H_1}\left(C_\tau)^{\frac{1}{2}}_{EQ_0} - \lambda C_\tau^{\frac{1}{2}}\right) + \left(\frac{\theta}{U_{1w}}\frac{dU_{1w}}{ds}\right)_{EQ}$$

$$- \frac{\theta}{U_{1w}}\frac{dU_{1w}}{ds}\left[1 + 0.075M^2 \frac{(1+0.2M^2)}{(1+0.1M^2)}\right]$$

where c_f is the skin friction coefficient in equilibrium flow in zero pressure gradient and λ is a scaling factor on the dissipation length. The suffix EQ denotes equilibrium conditions and EQ_0 equilibrium in the absence of secondary influences on turbulence structure.

Velocity Equation

$$(H+1)D\frac{\theta}{U_{1w}}\frac{dU_{1w}}{ds} = \frac{dH_1}{d\bar{H}}S + \frac{1}{2}c_f^*\left[(1+\tfrac{1}{5}M^2)H_1 - H\frac{dH_1}{d\bar{H}}\right]$$
$$- C_E(1+\tfrac{1}{5}M^2) .$$

The extraneous influences on the turbulence structure are contained in the scaling factor λ in the lag equation and the most important influence in this context is the effect of longitudinal curvature on turbulence structure for which λ is set to $1 + \beta_R R_i(1+M^2)/5$. Ri is the 'Richardson number' for which an average value through an equilibrium boundary layer is given approximately by

$$Ri = \frac{2}{3}\frac{\theta}{R}(H+H_1)\left(\frac{H_1}{\bar{H}} + 0.3\right) ;$$

β_R is taken from Ref 12 as 7 on a convex wall and 4.5 on a concave wall while R is the radius of longitudinal curvature.

The method is completed by the specification of a correlation between $\bar{H}$ and H_1 which can be derived from velocity profiles. For the calculation of separated flow velocity profiles must contain some reverse flow. The two parameter, low speed velocity-profile family of Le Balleur[18] and Lock[19] provides a suitable profile and is represented by the formula

$$\frac{U}{U_e} = 1 + C_1\log n - C_2 F(n)$$

where $n = y/\delta$ and $F(n)$ takes the form

$$F(n) = 0 \text{ if } 0 < n < n^* ,$$

$$F(n) = f(\frac{n-n^*}{1-n^*}) \text{ if } n^* < n < 1 ,$$

and n^* is zero for attached flows but defined empirically for separated flows. Lock found that a close fit to experimental profiles is obtained if f is taken as Coles' wake function, so that

$$f(\xi) = \tfrac{1}{2}(1+\cos\pi\xi)$$
where $\xi = (n-n^*)/(1-n^*)$.

These profiles can be used to determine a relationship between H and H_1 which is illustrated in Fig 14. Green[20] has argued that the 'transformed' shape parameter $\bar{H}$ might be regarded as the equivalent in compressible flows of the parameter H at low speeds, thus this (H, H_1) relationship can be used for compressible flows.

6.4 Viscous-inviscid Matching

A flow diagram for the semi-inverse method of matching the inner and outer flows is given in Fig 15. An initial estimate of the normalised transpiration velocity S is used in an inverse calculation of the boundary layer to give an estimate of the velocity distribution U_{1w}^V in the EIF. The same estimate is also used as a boundary condition in the direct inviscid method to yield another estimate U_{1w}^I of the velocity in the EIF. The difference between the two estimates of the

velocity, $U_{1w}^V - U_{1w}^I$, is used to correct the normalised transpiration velocity and the two simultaneous calculations are repeated. A stability analysis of a linearised form of the equations[14,21] which examines the growth of errors in the normalised transpiration velocity and streamwise velocity expressed as Fourier modes yields a correction formula for S,

$$\Delta S = \frac{\beta B \theta}{\beta + B \theta \pi / \Delta x} \left[\frac{1}{U_{1w}^V} \frac{dU_{1w}^V}{ds} - \frac{1}{U_{1w}^I} \frac{dU_{1w}^I}{ds} \right]$$

which proves useful in the full non-linear problem. The factor $\beta B \theta / (\beta + B \theta \pi / \Delta x)$ can be viewed as a relaxation factor which varies throughout the field of calculation and depends upon $\beta = \sqrt{(1-M^2)}$, Δx the panel length in the inviscid calculation and $B = (H+1)D \ dH/dH$, ie quantities from the boundary layer.

6.5 Outline of the Application of the Method

The method must be given the aerofoil ordinates, the Reynolds number, Mach number and angle of incidence. Then the laminar portion of the boundary layer is calculated by a compressible version of the method due to Thwaites[22]. The computer program allows for three different types of transition to a turbulent boundary layer. Natural transition is predicted by Granville's correlation[23]. If the laminar boundary layer separates before natural transition has been predicted then the development of the laminar separation bubble is calculated by Horton's semi-empirical method[24]. Transition can also be fixed at a specified point as long as neither of the other criteria has been satisfied upstream.

Downstream of transition the development of the boundary layer and wake are calculated by the inverse method described in Section 6.3.

7 Comparison Between Theory and Experiment

Calculations of the flow about a NACA 4412 aerofoil are compared with the experimental results at a Reynolds number of 4.17×10^6 and a Mach number of 0.18. In the theoretical calculation the transition from laminar to turbulent boundary layer is fixed at $x/c = 0.014$ and 0.110 on the upper and lower surfaces respectively, which correspond to the downstream ends of the transition trips used in the experiment. The theoretical method does not implicitly contain an estimate of the change in the state of the boundary layer as it passes over the trip, but this can be simulated by increasing the momentum thickness at the trip on the upper surface: at an angle of incidence of $12.15°$, which corresponds approximately to the maximum lift coefficient for the aerofoil in the experimental tests, an increase in the momentum thickness of the boundary layer of 0.0002 m at $x/c = 0.014$ on the upper surface leads to reasonable agreement with the momentum thickness measured at $x/c = 0.2$ and 0.4 as indicated in Fig 16. On the lower surface there is no increase in momentum thickness at the trip but the calculated value of 0.0008 m compares quite well with the measured value of 0.00064 m, at the trailing edge.

In the calculation of the turbulent boundary layer the effect on turbulence structure of longitudinal curvature has been included but the second order effects of flow curvature and Reynolds normal stress have not. Calculations with the same increase in momentum thickness at the upper surface trip are repeated for angles of incidence between 0° and 14.5°: the lift coefficients are compared with experimental and inviscid values in Fig 17. Up to an incidence of 12.15°, there is good agreement with the experimental results. However the theoretical results extend beyond the range of experimental values and indicate a decrease in the lift coefficient as the separation point moves towards the leading edge. The calculated and measured pressure distributions at an angle of incidence of 12.15° are compared in Fig 18. The interaction calculation was run for 200 iterations so that it is fully converged in terms of lift coefficient. The two pressure distributions are similar except that the experiment indicates slightly lower pressures in two regions: from $0.05 < x/c < 0.4$ on the upper surface and on the aft parts of both surfaces. In the latter case the shape of the predicted pressure distribution is, however, correct in the main and the differences in level may be ascribed to differences between the measured and predicted separation positions. Using the experimentally-supported criterion (Section 5) that a shape parameter of four identifies the point of separation (ie the first appearance of reversed flow in the time-mean velocity profile), then separation in the experiment occurs just ahead of $x/c = 0.80$ whilst in the calculation it occurs just ahead of $x/c = 0.90$.

There are several possible explanations for the differences between theory and experiment: the change in momentum thickness at the transition trip could be incorrect; the tunnel interference induces a camber in the flow; the three-dimensional nature of the flow in the wind tunnel, and perhaps its slight unsteadiness, might be equivalent to a change in the effective incidence of the model; or there may be significant deficiencies in the shear layer calculations such as the omission of normal stress terms. The importance of the first three of these possibilities has been checked by appropriate calculations.

Increasing the momentum thickness at the trip by 0.0003 m instead of 0.0002 m moves the separation point forward to $x/c = 0.82$ but the lift coefficient falls to 1.38 which is some 6% below the experimental value.

Using Fig 1, the flow curvature and inclination induced by tunnel interference have been counteracted by adding an opposing camber to the aerofoil and slightly increasing its incidence. The pressure distribution about the distorted aerofoil at the corrected incidence has been compared with the uncorrected pressure distribution. Separation moved forward to $x/c = 0.86$ and the consequent reductions in pressure near the trailing edge contributed to a slight (1.4%) increase in lift coefficient, but there was no noticeable improvement in the pressure distribution closer to the leading edge.

A calculation at an angle of incidence of 13.5° (without an induced camber correction) gave much closer agreement with the experimental pressure distribution as shown in Fig 19. The point of

separation moved forward to x/c = 0.79 and the
lift coefficient increased slightly to 1.490 which
is still close to the experimental value. The
displacement thicknesses from experiment and
calculation at angles of incidence of 12.15° and
13.5° are compared in Fig 20. The calculations at
the higher incidence much more closely reflect the
trend of the measurements. This is to be expected
in view of the effect of the incidence change on
the pressure distribution. However the measured
momentum thicknesses are better represented by the
calculation at the lower incidence (Fig 16) for
the rear part of the wing. In this region the
measured shape parameter (H), which depends on
both thicknesses, consequently falls between the
calculated results for the two incidences
(Fig 21).

It is suggested that further analysis is required
before the discrepancy between measured and calcu-
lated momentum thicknesses can be properly
assessed. On the one hand the effect of using the
generalised definition[8] to evaluate the experimen-
tal values needs to be estimated and on the other
the effects of Reynolds normal stresses need to be
included in the calculations.

8   Concluding Remarks

The flow near a stalling NACA 4412 aerofoil has
been studied both experimentally and theoreti-
cally. The experimental results yield a fairly
detailed picture of the flow around the aerofoil
and in the upstream part of its wake. The results
emphasise how the shear flow near the rear of the
aerofoil alters the effective thickness and camber
of the disturbance that the aerofoil introduces
into the free stream. They also confirm that the
shear layers near and beyond separation are thick
enough to require a higher order theoretical
treatment than traditional boundary layer theory.

Comparison of the experiment with a semi-inverse,
viscous-inviscid-interaction theory shows that
lift coefficients for this aerofoil can be pre-
dicted very well up to and rather beyond maximum
lift. Predictions of detailed pressure distribu-
tions near maximum lift are slightly less
accurate, though the level of agreement with
experiment is very encouraging.

Several possible reasons for the discrepancies
between theory and experiment have been advanced
and, in some cases, their likely importance has
been tested by calculation. However, it is not
clear to what extent the discrepancies are attri-
butable to imperfections in the experiment or to
the need for better representations of separating
shear layers in the theory. The further develop-
ment of this empirical aspect of the theory, if
indeed it is significantly in error, will depend
on the availability of suitable experimental data,
such as those presented here, for detailed
analysis.

REFERENCES

1   R.C. Lock, M.C.P. Firmin. Survey of tech-
    niques for estimating viscous effects in
    external aerodynamics.
    Numerical Methods in Aeronautical Fluid
    Dynamics, ed P.L. Roe, Academic Press (1982).

2   B.R. Williams. The prediction of separated
    flow using a viscous-inviscid interaction
    method.
    ICAS-84-2.3.3 (1984).

3   A.J. Wadcock. Flying hot-wire study of a two-
    dimensional turbulent separation on a NACA
    4412 airfoil at maximum lift.
    Ph D thesis, California Institute of
    Technology (1978).

4   R.C. Hastings, K.G. Moreton, R. Clark. Mean
    flow properties measured around an aerofoil
    close to its maximum lift.
    Paper 14-1. 2nd Int. Symp. on Appl. of Laser
    Anemometry to Fluid Mechanics, Lisbon
    July 2-4 (1984).

5   A.E. Winkelmann. On the occurrence of
    mushroom shaped stall cells in separated flow.
    AIAA Paper 83-1734 (1983).

6   D.A. Lovell. An automatic wake traverse
    system for flow field measurements in large
    low-speed wind tunnels.
    RAE TR 80078 (1980).

7   P.R. Ashill, D.J. Weeks. A method for deter-
    mining wall-interference corrections in solid-
    wall tunnels from measurements of static
    pressure at the walls.
    Paper 1, AGARD CP No 335 (1982).

8   L.F. East. A representation of second-order
    boundary layer effects in the momentum
    integral equation and in viscous-inviscid
    interactions.
    RAE TR 81002 (1981).

9   J.E. Green. Two-dimensional turbulent reat-
    tachment as a boundary layer problem.
    RAE TR 66059 (1966).

10 S.J. Kline, J. Bardina, R. Strawn.
    Correlation and computation of detachment and
    reattachment of turbulent boundary layers on
    two-dimensional faired surfaces.
    AIAA-81-1220 (1981).

11 L.F. East, P.D. Smith, P.J. Merryman.
    Prediction of the development of separated
    turbulent boundary layers by the lag-
    entrainment method.
    RAE TR 77046 (1977).

12 J.E. Green, D.J. Weeks, J.W.F. Brooman.
    Prediction of turbulent boundary layers and
    wakes in compressible flow by a lag-
    entrainment method.
    ARC R&M 3791 (1977), also RAE TR 72231 (1972).

13 J.E. Carter. A new boundary layer inviscid
    interaction technique for separated flows.
    AIAA-79-1450 (1979).

14   J.C. Le Balleur. Couplage visqueux - non
     visqueux: méthode numérique et applications
     aux écoulements bidimensionnels transsoniques
     at supersonique.
     La Recherche Aérospatiale, 1978-2 (1978).

15   B.R. Williams. The calculation of separated
     flows for a two-dimensional aerofoil at low
     speed.
     RAE TR to be published.

16   J.C. Newling. An improved two-dimensional
     multi-aerofoil program.
     HSA-MAE-R-FOM-0007 (1977).

17   D.J. Weeks. RAE unpublished paper.

18   J.C. Le Balleur. Strong matching method for
     computing transonic viscous flows including
     wakes and separations on lifting aerofoils.
     La Recherche Aérospatiale, 1981-3 (1981).

19   R.C. Lock. Private communication.

20   J.E. Green. The prediction of turbulent boun-
     dary layer development in compressible flows.
     J Fluid Mech., 31, 753-778 (1968).

21   L.B. Wigton, M. Holt. Viscous-inviscid
     interaction in transonic flow.
     AIAA-81-1003 (1981).

22   B. Thwaites (Ed). Incompressible
     aerodynamics.
     Clarendon Press (1960).

23   P.S. Granville. The calculation of viscous
     drag of bodies of revolution.
     David Taylor Model Basin, Report 849 (1953).

24   H.P. Horton. A semi-empirical theory for the
     growth and bursting of laminar separation
     bubbles.
     ARC CP 1673 (1967).

Reports quoted are not necessarily available
to members of the public or commercial
organisations.

TABLE 1

TUNNEL ROOF AND FLOOR PRESSURE COEFFICIENTS

*x/c	$(C_p)_{Roof}$	$(C_p)_{Floor}$
-1.0	-0.079	+0.106
-0.8	-0.111	0.127
-0.6	-0.157	0.147
-0.4	-0.193	0.168
-0.2	-0.226	0.188
0	-0.256	0.190
+0.2	-0.288	0.190
0.4	-0.282	0.186
0.6	-0.270	0.170
0.8	-0.234	0.159
1.0	-0.202	0.131
1.2	-0.166	0.107
1.4	-0.134	0.089
1.6	-0.099	0.040

*Along the tunnel axis, here only.

Fig 13

Constant source strength, σ_i

Linearly varying vorticity, γ_i

$\sigma_{\frac{N}{2}}$

$\gamma_{\frac{N}{2}+1}$

γ_3 σ_2 γ_2 σ_1 γ_1

γ_3 σ_2 γ_2 σ_1

Constant source strength

N-sided inscribed polygon
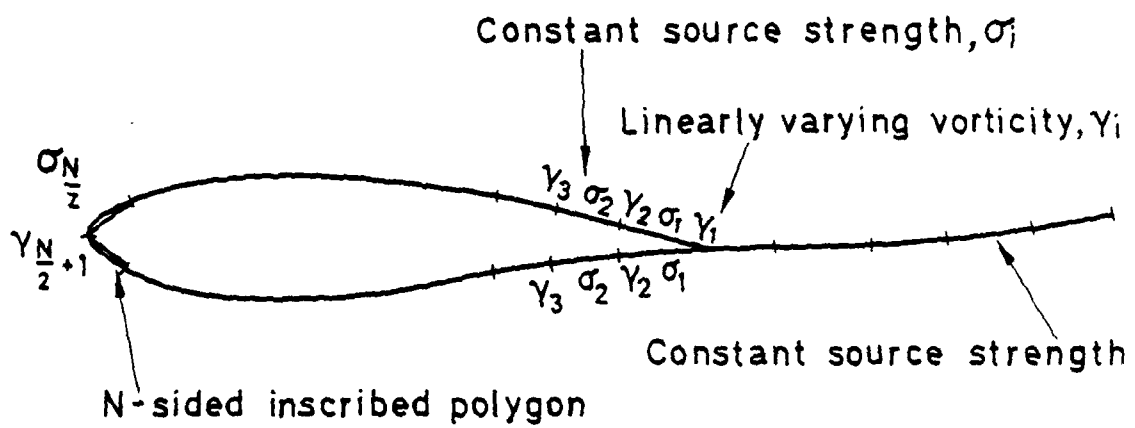
Singularities are equal on
upper and lower surfaces

Fig 13   Singularity model used in panel method

T Memo Aero 2026

Fig 12

$$W_{iw} = \frac{1}{\rho_{iw}} \frac{d}{ds} (\rho_{iw} U_{iw} \delta^*)$$

$$\Delta W_i = \frac{1}{\bar{\bar{\rho}}_{iw}} \frac{d}{ds} (\bar{\bar{\rho}}_{iw} \bar{\bar{U}}_{iw} \delta^*_t)$$

Dividing
streamline

$$\Delta U_i = -K_w \bar{\bar{U}}_{iw} (\delta^*_t + \Theta_t)$$

Free stream

Pressure correction
$\sim K^*(\Theta + \delta^*)$
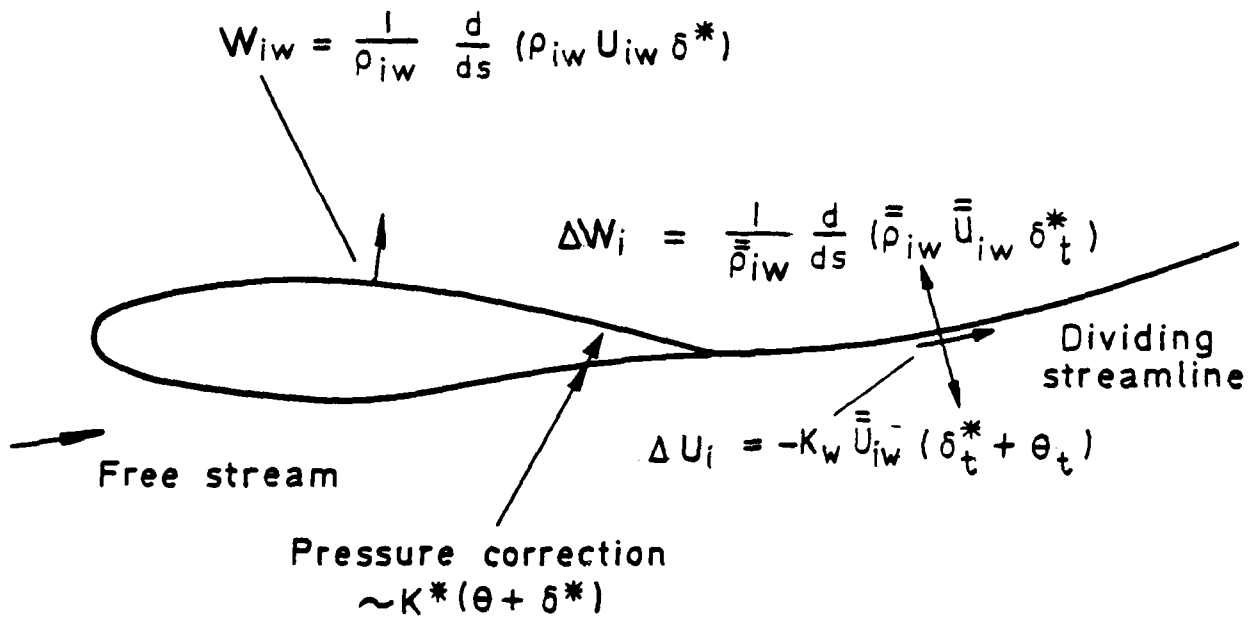
Fig 12 Boundary conditions and corrections for EIF

Fig 11

T Memo Aero 2026
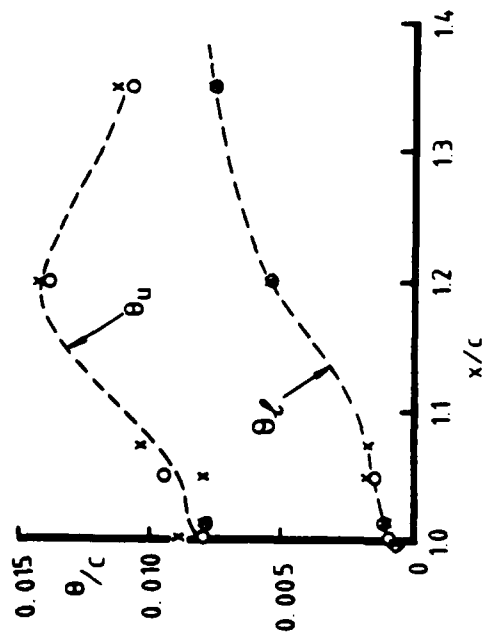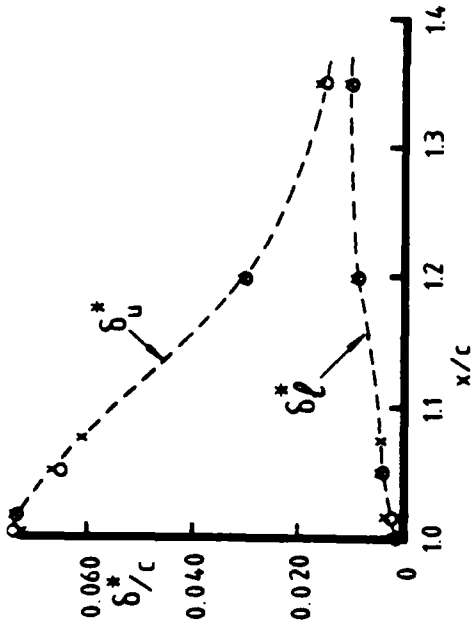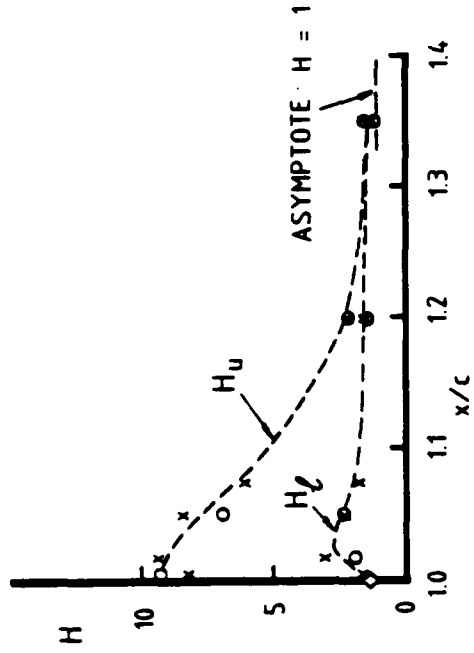
ASYMPTOTE · H = 1

Fig. 11 Integral properties of wake

Fig 10
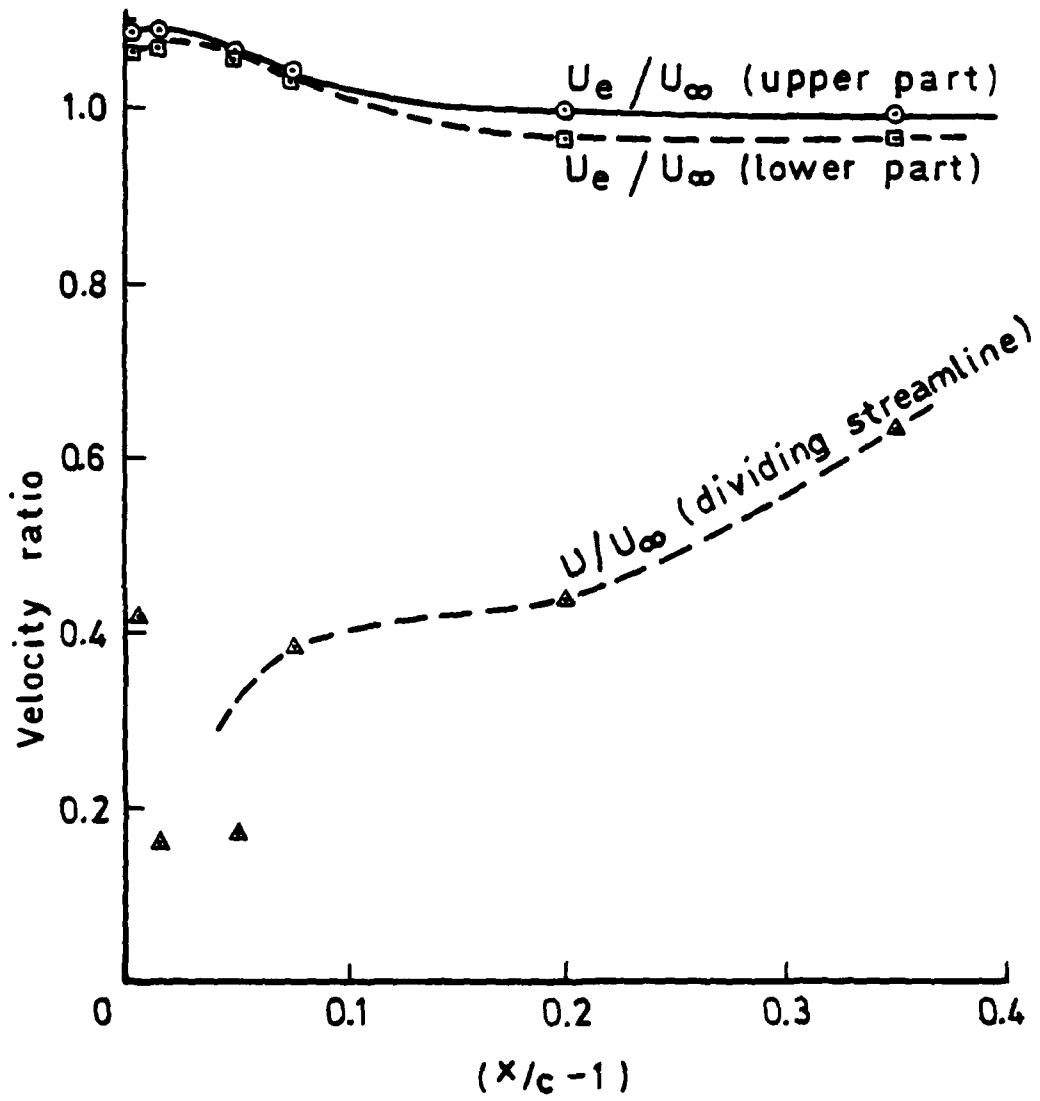
Fig 10   Wake edge and dividing streamline
velocities

Fig 9
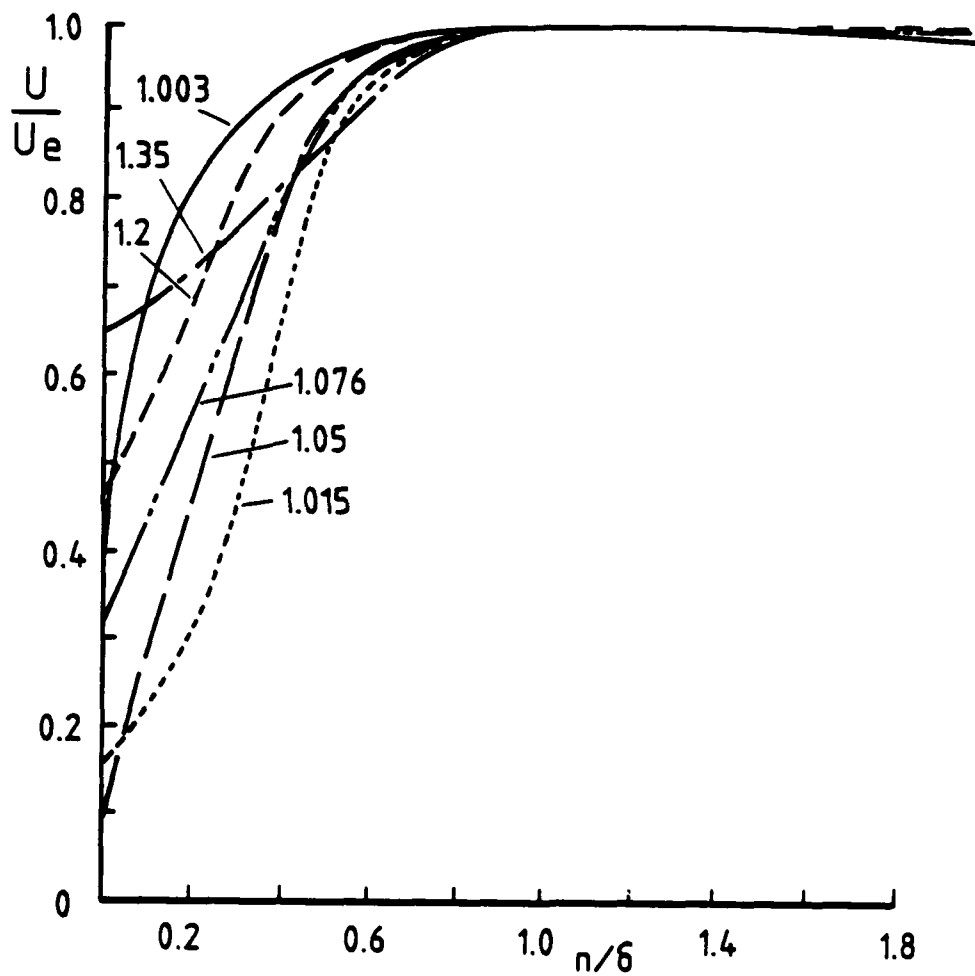
Fig. 9   Normalised wake velocity profiles
         (lower)

Fig 8
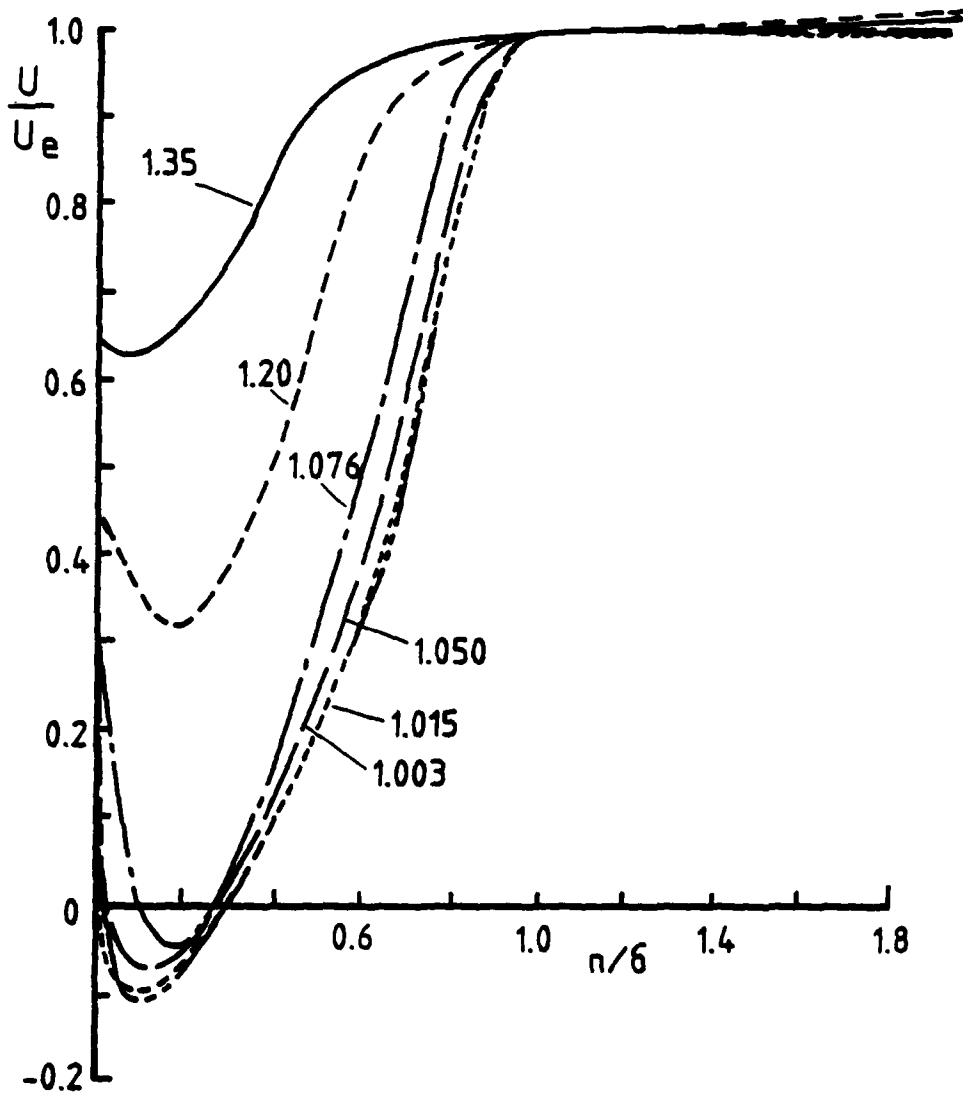
Fig. 8   Normalised wake velocity profiles
(upper)

Fig 7
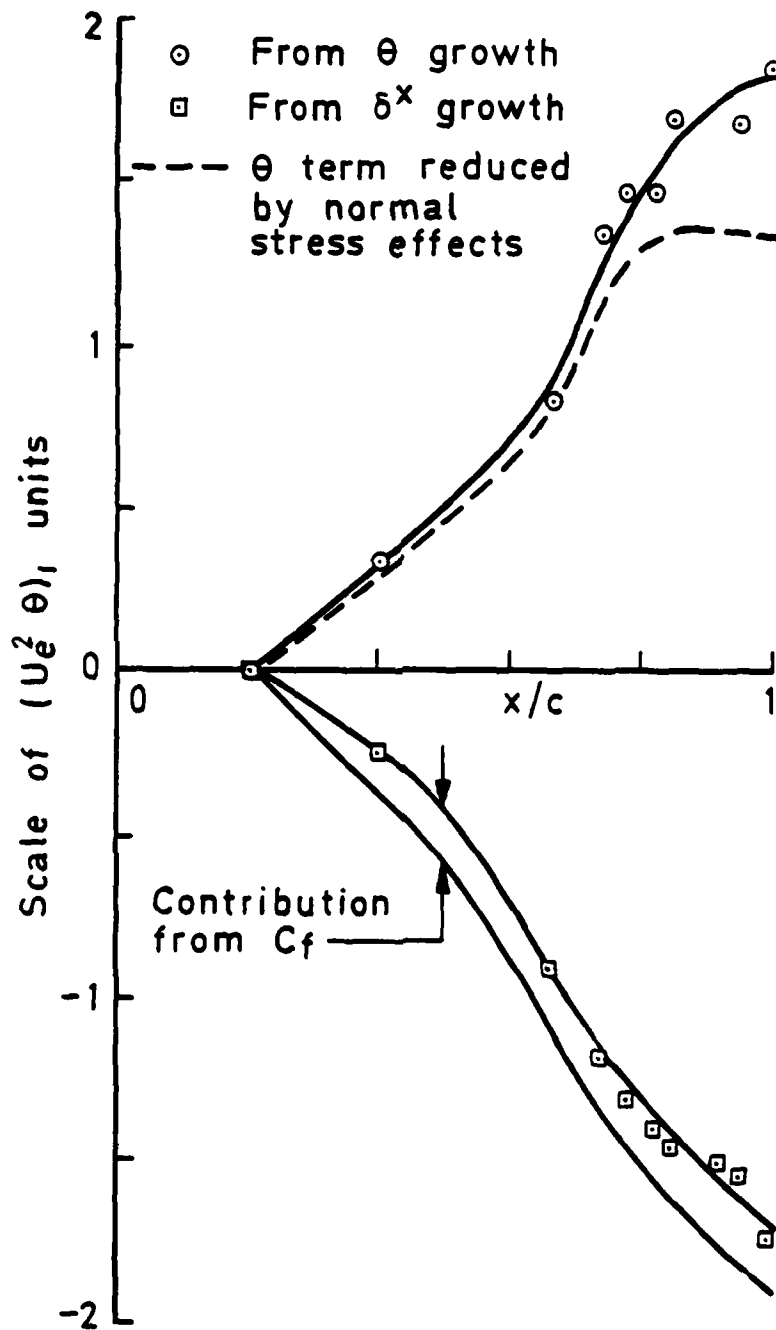
Fig 7 First-order momentum balance for upper surface boundary layer

Fig 6
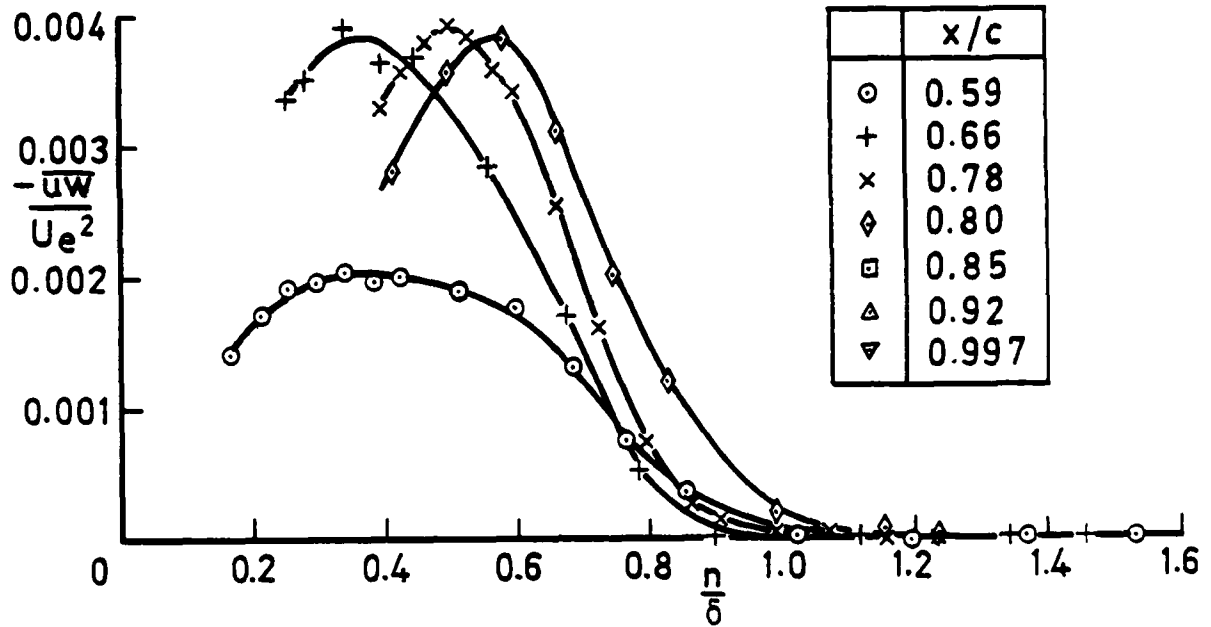
(a) $0.59 \leqslant x/c \leqslant 0.80$
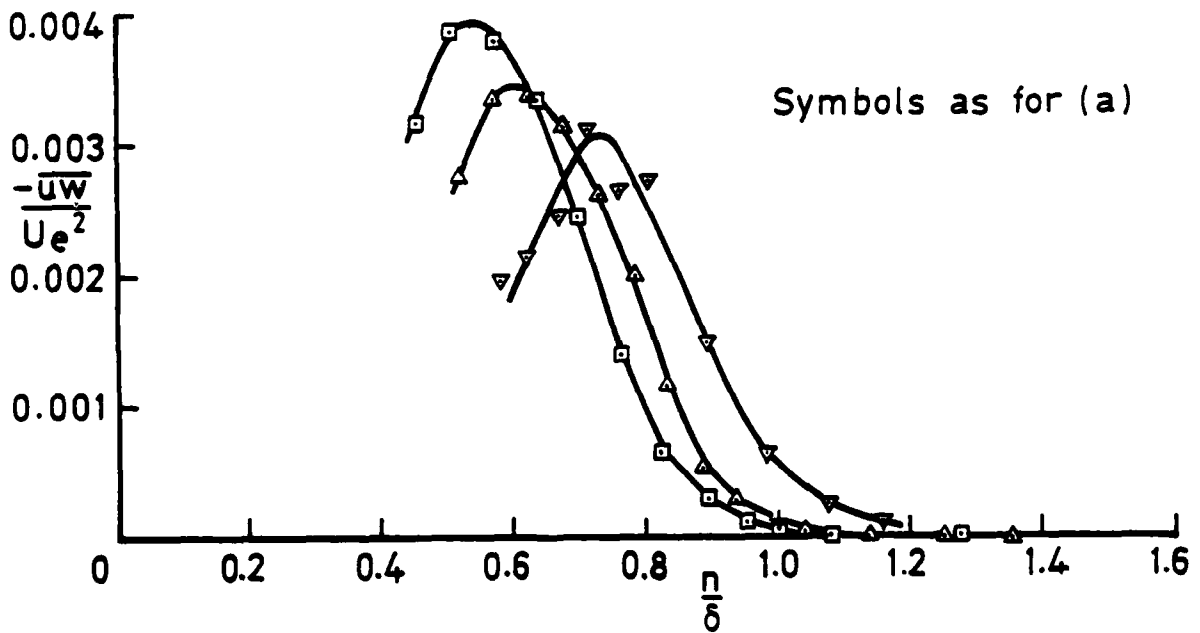
(b) $0.85 \leqslant x/c \leqslant 0.997$

Fig 6 Dimensionless shear stress

Fig 5
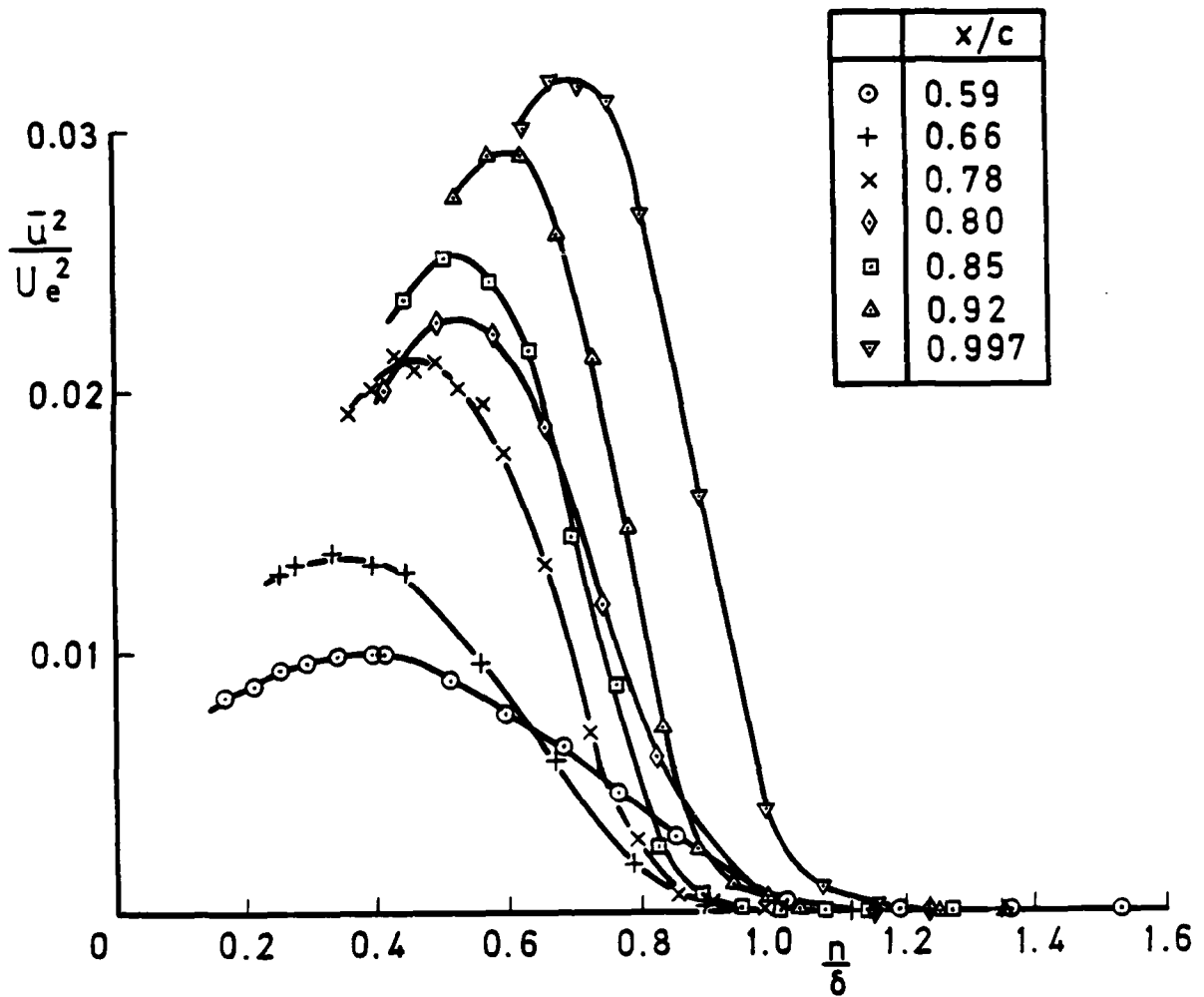
(a) Longitudinal normal stress
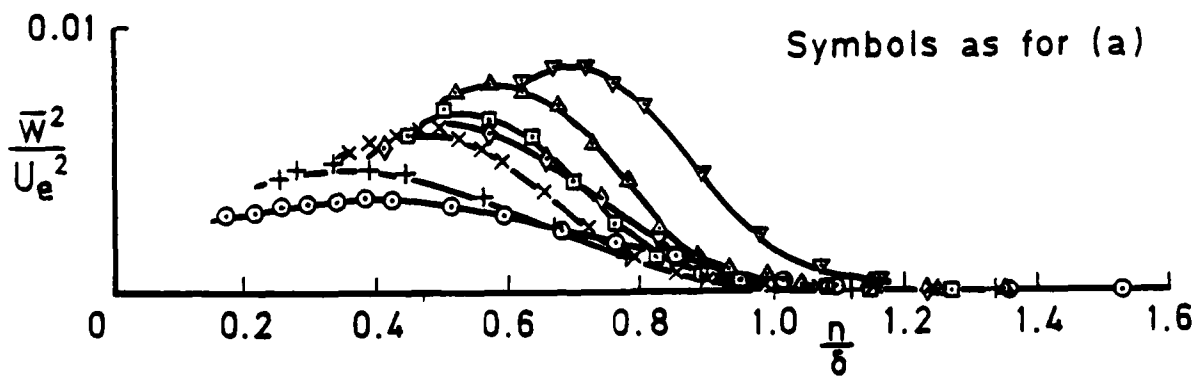
(b) Outward normal stress

Fig 5 Dimensionless Reynolds normal stresses
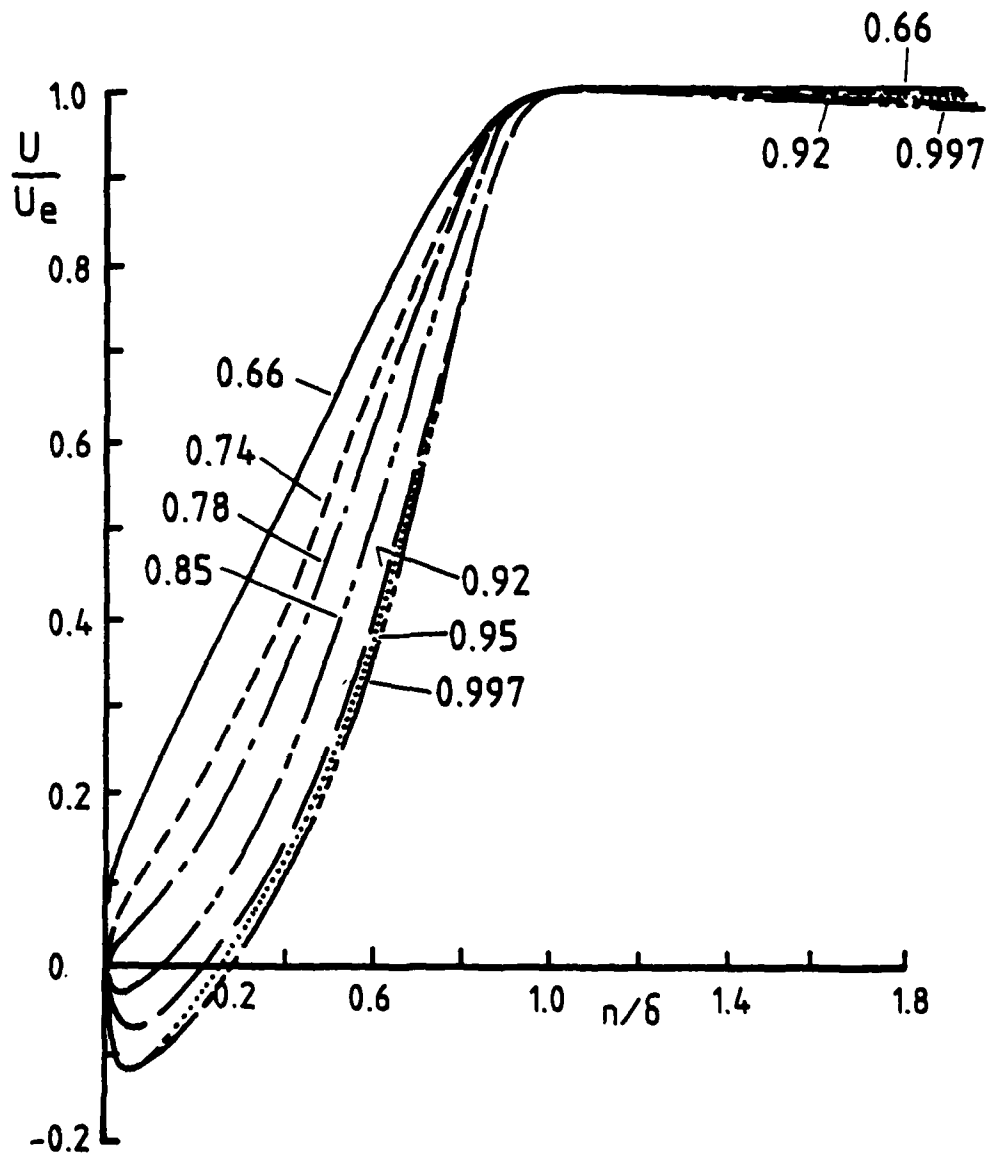
Fig 4

Fig. 4   Upper surface velocity profiles
         (x/c ≥ 0.66)

Fig 3

T Memo Aero 2026

x/c ≈ 0.95		
	Fringe direction	Test date
◁ ◇	± 45° 0,90°	7/83
× O	± 45° 0,90°	4/84
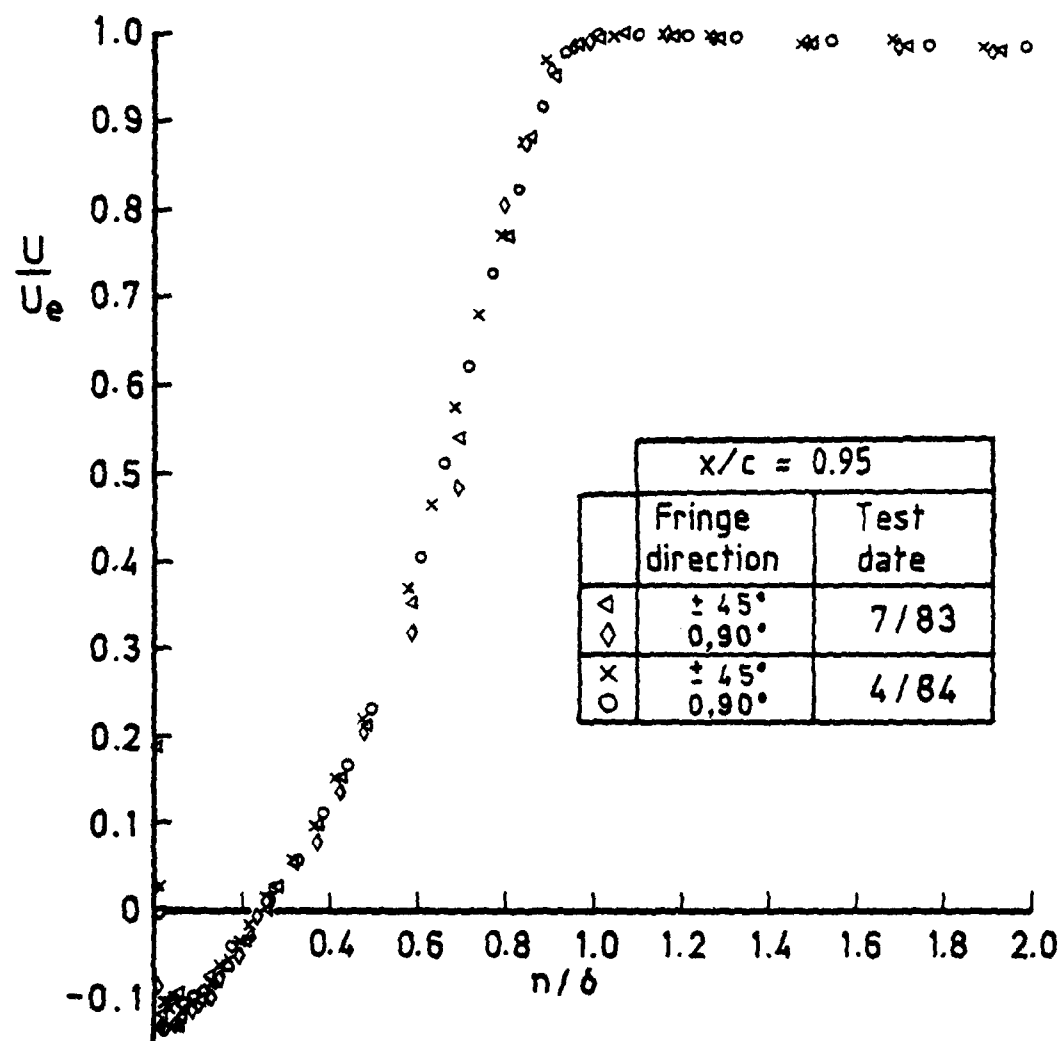
Fig 3   LDA separated flow profile data

Fig 2
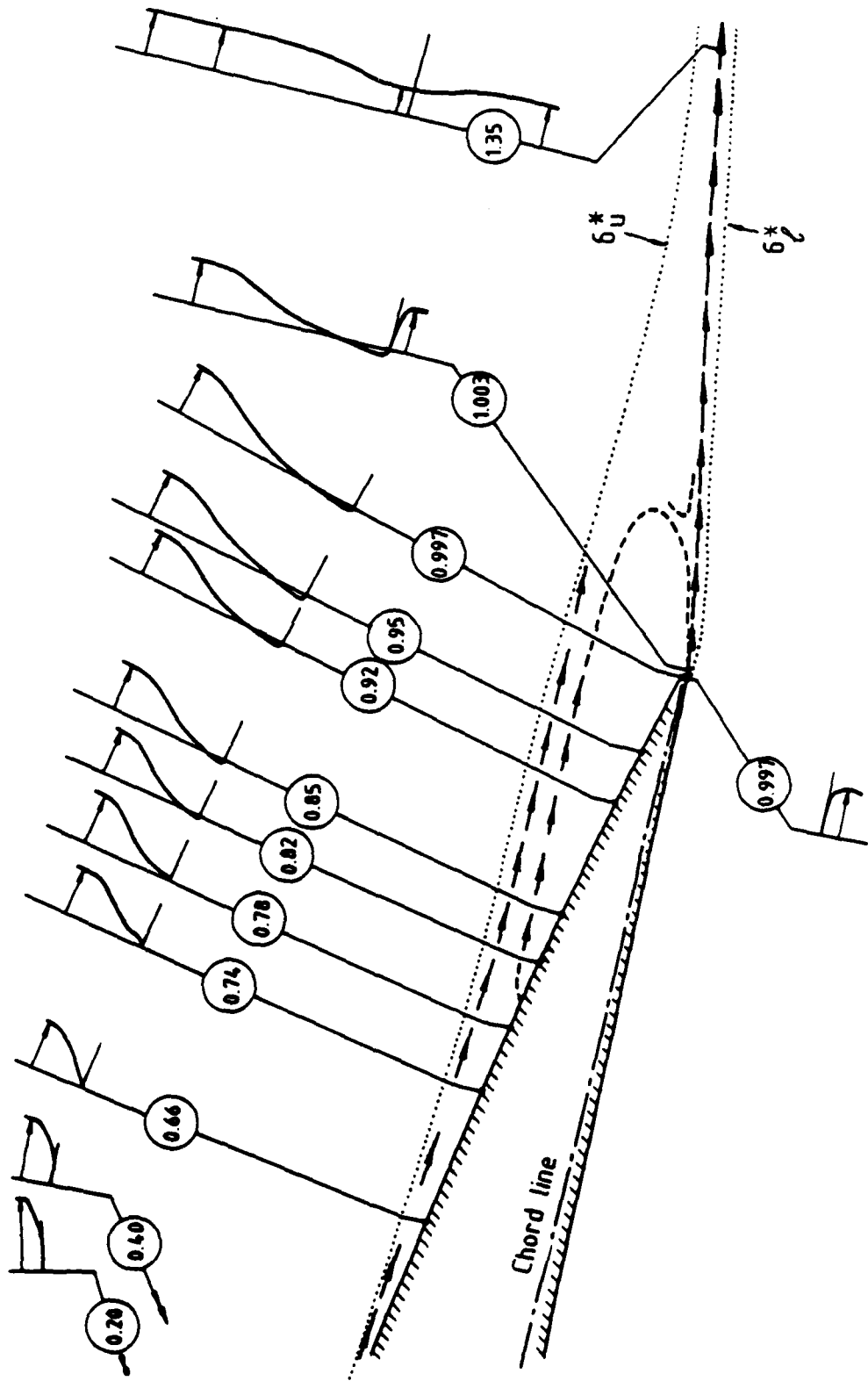
Fig. 2 Flow near trailing edge of aerofoil for $\alpha = 12.15°$

T Memo Aero 2026
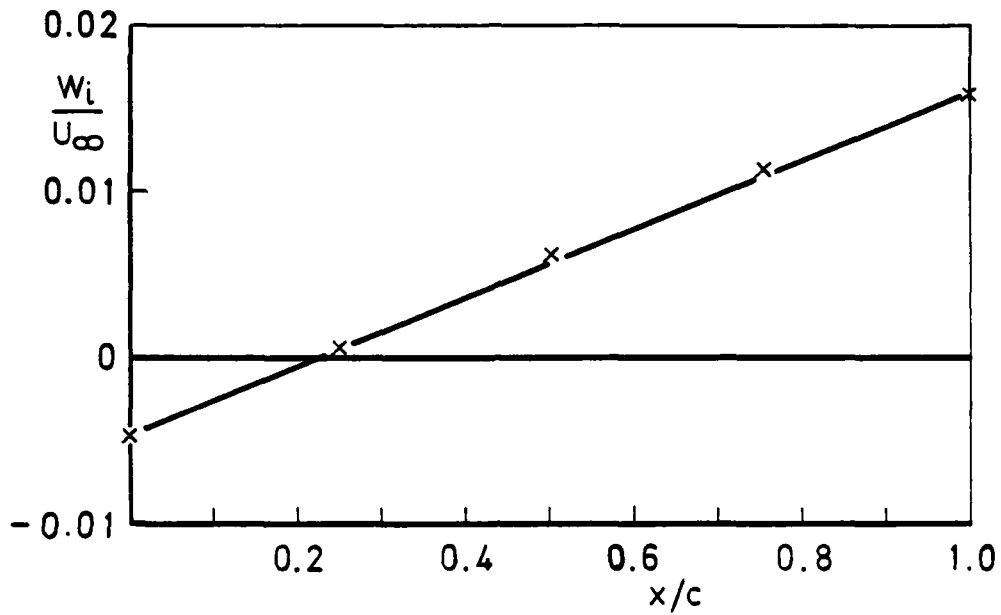
Fig 1

(a) Induced upwash along the chord
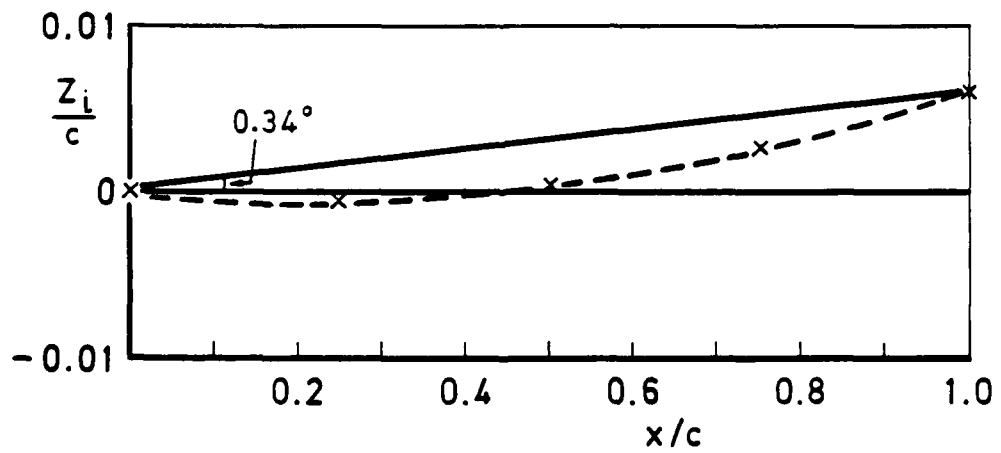
(b) Induced camber of flow

Fig 1 Wall interference effects on tunnel axis

TABLE 2

BOUNDARY LAYER CHARACTERISTICS

x/c	$(C_p)_{Wall}$	δ/c $(U/U_e=0.995)$	H	θ/c	R_θ	$(C_\tau)_{Max}$	$(C_f)_{Est}$	$(I/\theta)_{Est}$
				(Upper Surface)				
0.20	−1.875	0.0085	1.54	0.00119	8455	−	0.00190	0.021
0.40	−1.160	0.0141	1.59	0.00210	12920	−	0.00155	−
0.59	−0.5863	0.022	−	−	−	0.0041	$(75\pm15)\times10^{-5}$	0.027
*0.66	−0.4192	0.0286	2.64	0.00439	21755	0.0077	$(22\pm8)\times10^{-5}$	0.036
0.74	−0.2943	0.0420	3.11	0.00618	29450	−	$(6\pm2)\times10^{-5}$	−
0.78	−0.2539	0.0490	3.63	0.00674	31560	0.0078	$(3\pm1)\times10^{-5}$	0.053
0.80	−0.2418	0.054	−	−	−	0.0077	−	−
*0.82	−0.2311	0.0600	4.71	0.00683	30350	−	−	0.082
0.85	−0.2230	0.0650	4.97	0.00753	34430	0.0079	−	0.104
0.92	−0.2145	0.0814	6.67	0.00786	35165	0.0070	−	0.143
0.95	−0.2100	0.0935	8.13	0.00757	33985	−	−	−
0.997	−0.190	0.1077	8.72	0.00821	35840	0.0062	−	0.184
				(Lower Surface)				
0.997	−0.140	0.0078	1.275	0.000636	2690	$(= c_f)$	0.00395	−

*Early LDA Profile Data

TABLE 3

WAKE CHARACTERISTICS

x/c	U_e/U_∞	δ/c $(U/U_e=0.995)$	H	θ/c	z/c	U/U_∞
	(above dividing streamline)				(on dividing streamline)	
1.003	1.088	0.1085	8.70	0.00842	−0.00130	0.417
1.015	1.089	0.1075	9.32	0.00789	−0.00131	0.160
1.050	1.067	0.1014	7.65	0.00867	+0.00537	0.170
1.076	1.040	0.1052	5.96	0.01029	0.0102	0.385
1.200	0.993	0.0935	2.18	0.01399	0.0352	0.436
1.350	0.990	0.0960	1.37	0.01092	0.0633	0.631
	(below dividing streamline)					
1.003	1.068	0.0105	1.57	0.00093		
1.015	1.073	0.0086	2.44	0.00108		
1.050	1.061	0.0152	2.33	0.00159		
1.076	1.035	0.0156	1.74	0.00174		
1.200	0.961	0.0580	1.50	0.00547		
1.350	0.962	0.0665	1.31	0.00756		

Fig 14
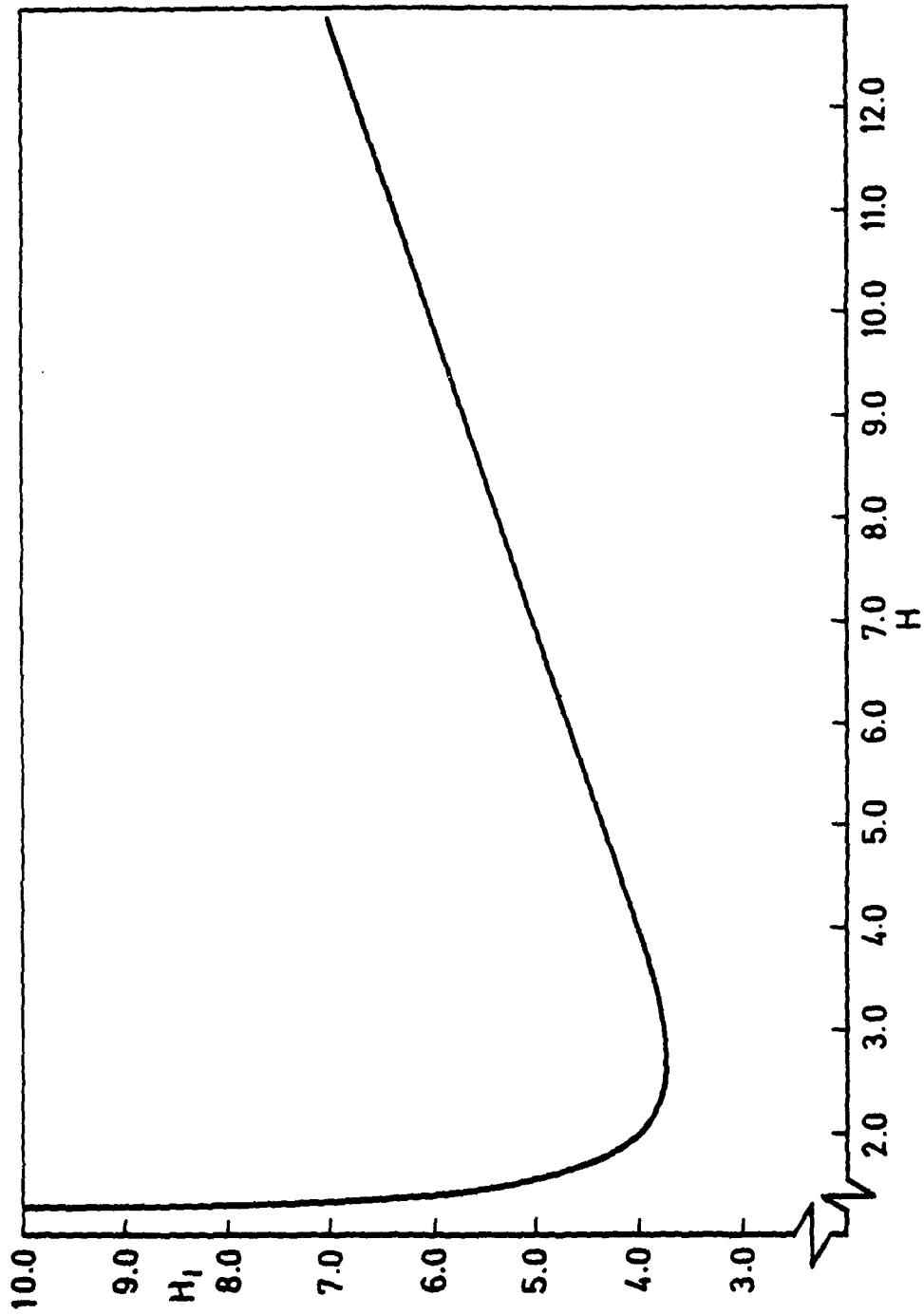

Fig 14 (H,H₁) correlation for two-parameter velocity profile family

Fig 15
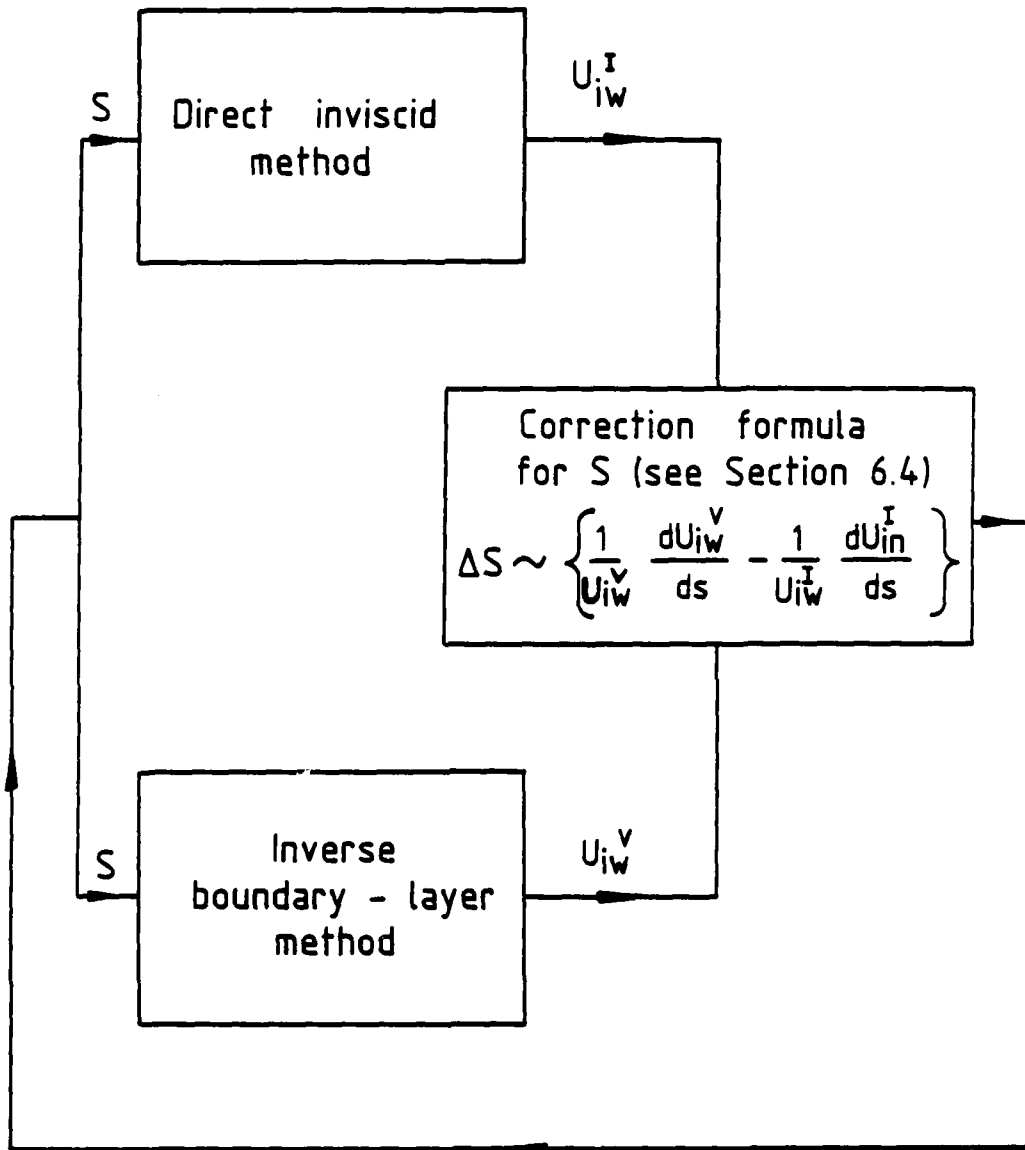

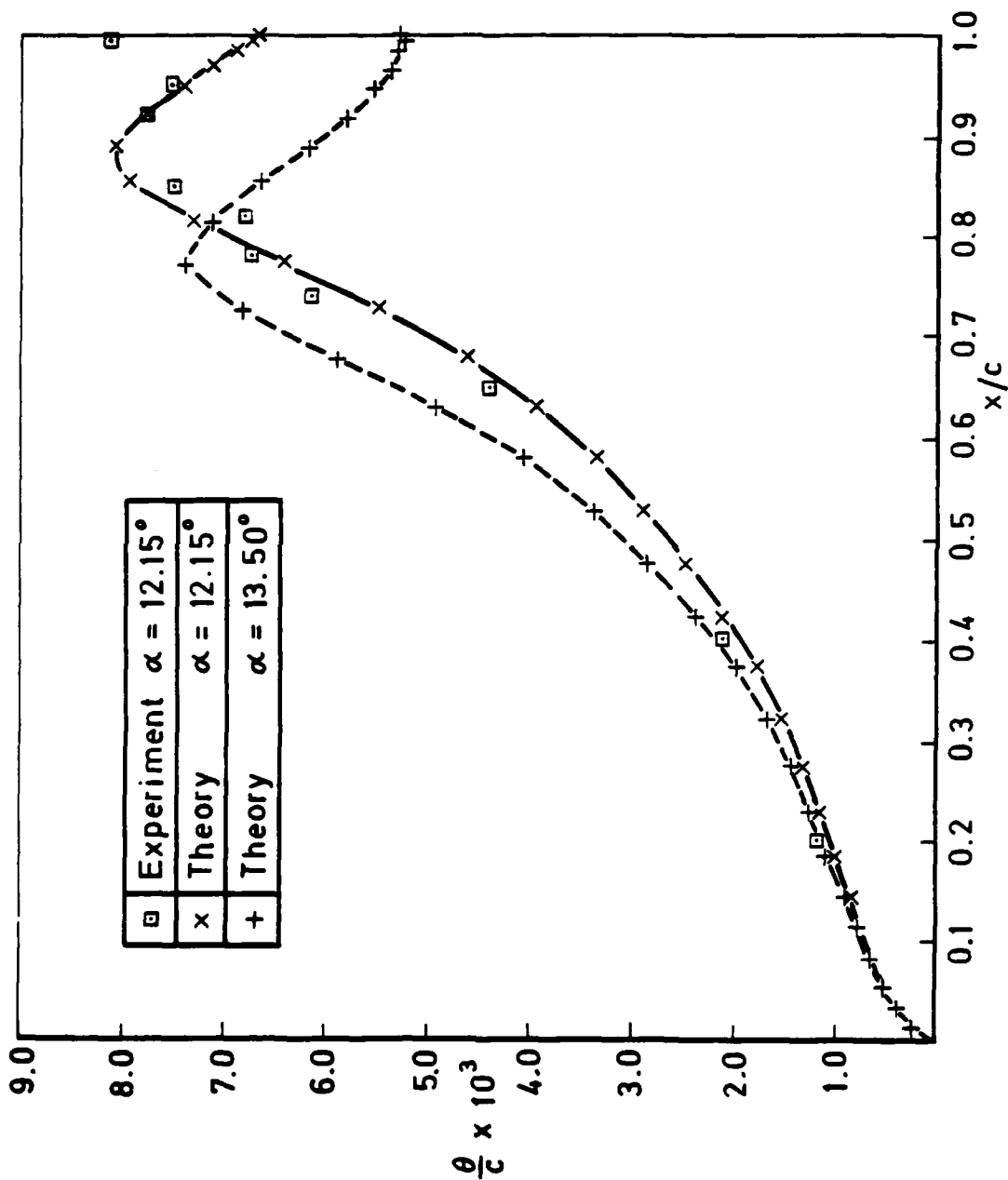
Fig. 15   Flow diagram for semi – inverse method

Fig 16

Fig 16 Development of θ/c on upper surface

Fig 17

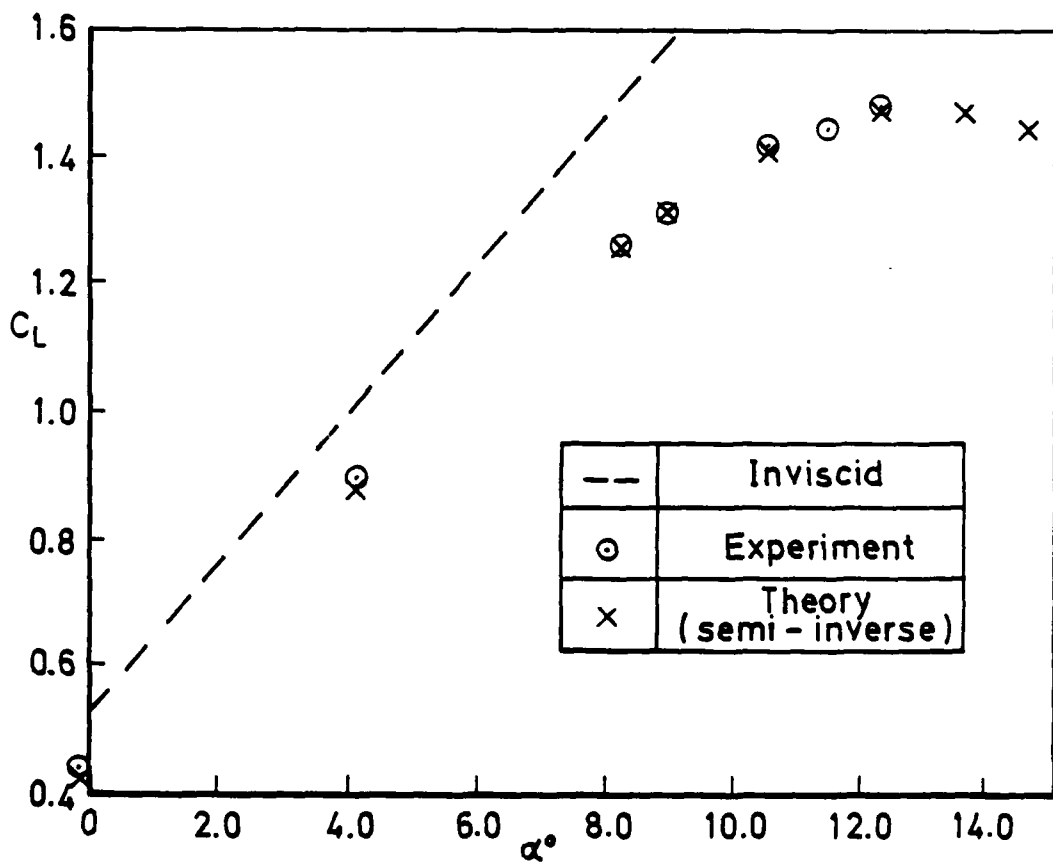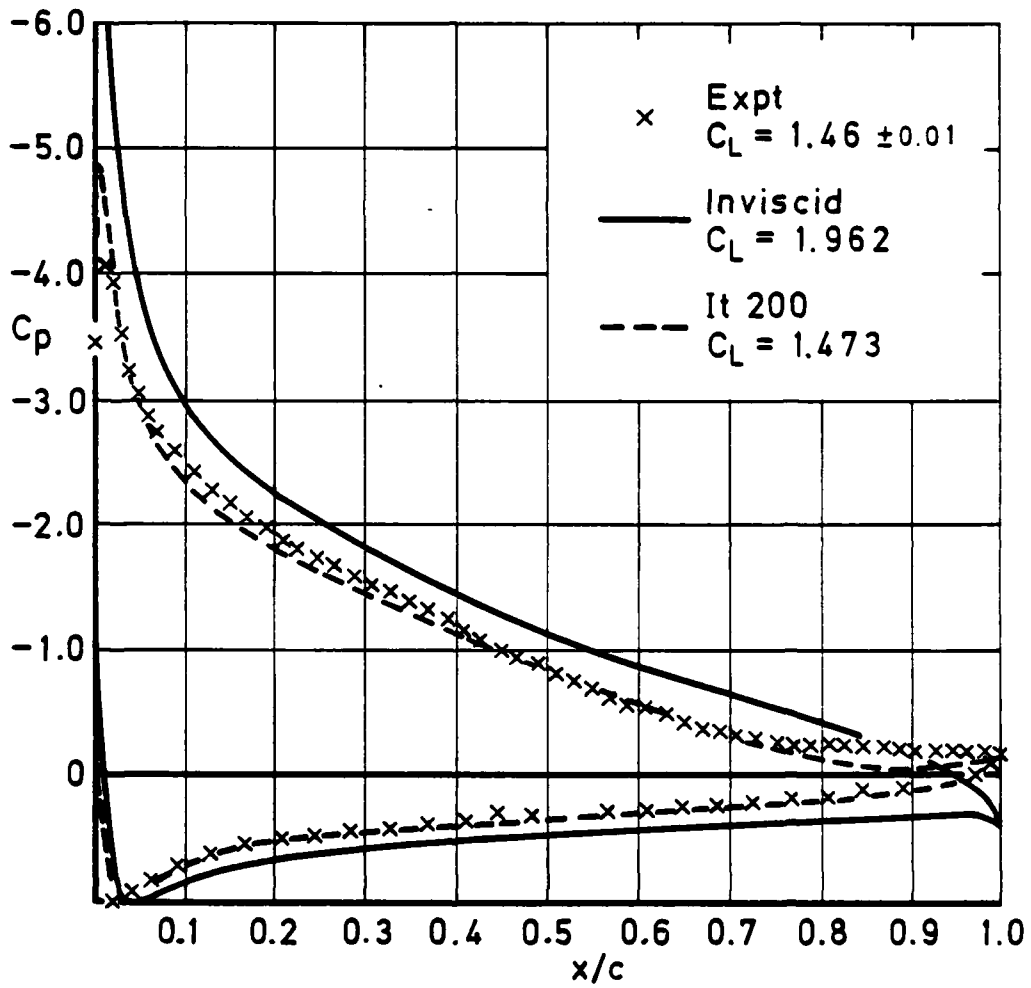Fig 17   Variation of C_L with α for present test

Fig 18

Fig 18   Aerofoil pressure distribution
at $\alpha = 12.15°$

Fig 19

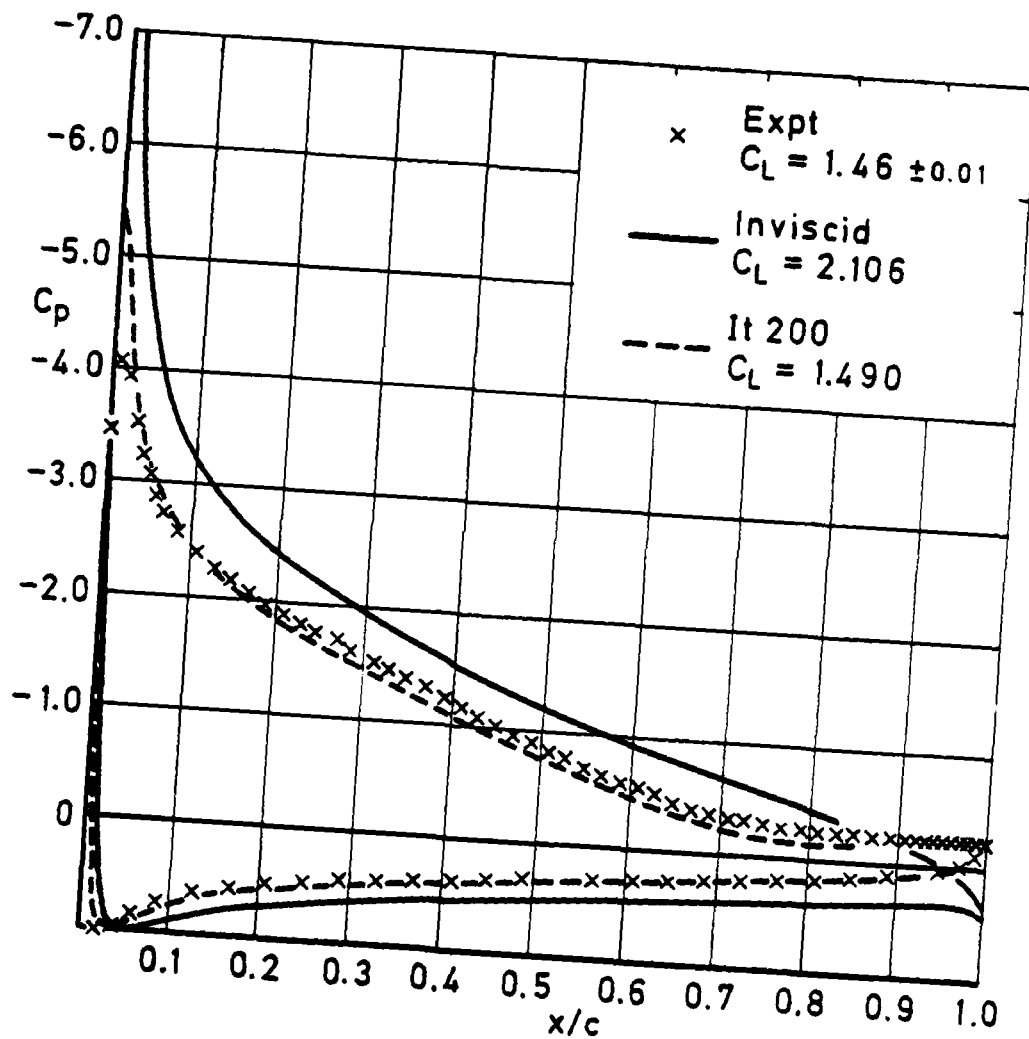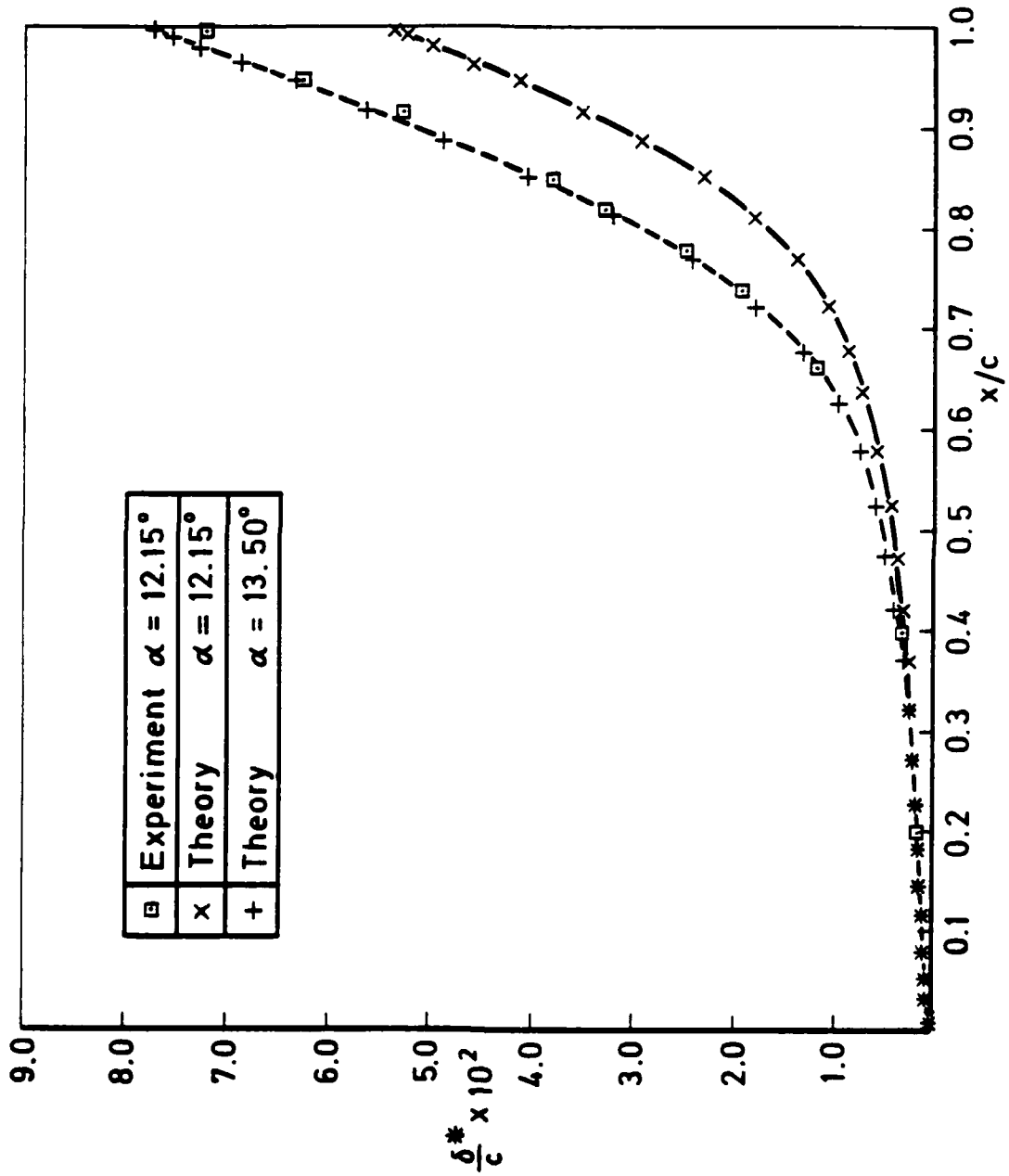Fig 19   Computed pressure distribution
at $\alpha = 13.5°$

Fig 20

Fig 20 Development of δ^*/c on upper surface
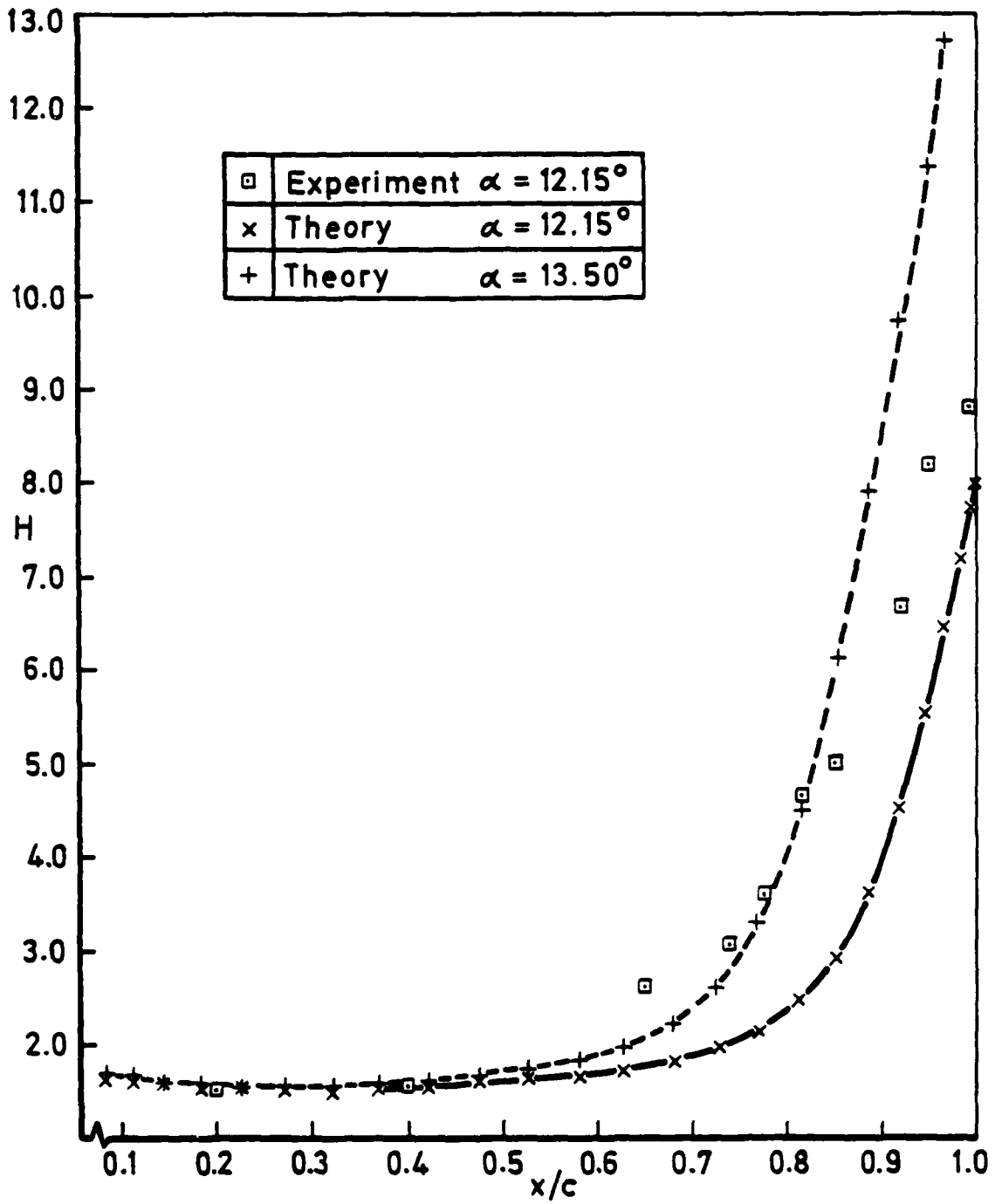
Fig 21

Fig 21 Development of H on upper surface

REPORT DOCUMENTATION PAGE

Overall security classification of this page

UNCLASSIFIED

As far as possible this page should contain only unclassified information. If it is necessary to enter classified information, the box above must be marked to indicate the classification, e.g. Restricted, Confidential or Secret.

1. DRIC Reference (to be added by DRIC)	2. Originator's Reference	3. Agency Reference	4. Report Security Classification/Marking
	RAE TM Aero 2026		UNCLASSIFIED UNLIMITED

5. DRIC Code for Originator	6. Originator (Corporate Author) Name and Location
7672000H	Royal Aircraft Establishment, Bedford, Beds, UK

5a. Sponsoring Agency's Code	6a. Sponsoring Agency (Contract Authority) Name and Location

7. Title Studies of the flow field near a NACA 4412 aerofoil at nearly maximum lift

7a. (For Translations) Title in Foreign Language

7b. (For Conference Papers) Title, Place and Date of Conference

8. Author 1. Surname, Initials	9a. Author 2	9b. Authors 3, 4	10. Date	Pages	Refs.
Hastings, R.C.	Williams, B.R.		December 1984	34	24

11. Contract Number	12. Period	13. Project	14. Other Reference Nos.

15. Distribution statement
(a) Controlled by --

(b) Special limitations (if any) --

If it is intended that a copy of this document shall be released overseas refer to RAE Leaflet No.3 to Supplement 6 of MOD Manual 4.

16. Descriptors (Keywords)   (Descriptors marked * are selected from TEST)
Two-dimensional flow*. Turbulent boundary layers*; Subsonic; Flow separation; Aerofoil flow. (Great Britain)

17. Abstract

END

DATE
FILMED

9 -85